

Master's Thesis

**Extended non linear dynamics for quadrotor control in
aggressive maneuvering**

H.J.K. de Kleuver

DC 2017.092

Coach: dr. ir. A.A.J. Lefeber
Supervisor: prof. dr. H. Nijmeijer

Eindhoven, October, 2017

Dynamics and Control
Department of Mechanical Engineering
Eindhoven University of Technology
PO Box 513
5600 MB Eindhoven
The Netherlands

Abstract

Lately, the trend in development of drone applications increasingly focuses on cooperation between drones. For collision avoidance the drones in the formation need to accurately follow their trajectory. Previous work on this topic resulted in a quadrotor capable of tracking a trajectory, however, while in slow varying trajectories the tracking performance is good, in fast varying trajectories the performance significantly decreases. Adjustments to the previous work are required to improve the tracking performance for all flight cases. The main objective of this thesis is to improve the tracking performance by improving the quadrotor's dynamical model and perform a redesign of the controller to account for the new dynamics. A partially improved controller, designed by van der Eijnden and Lefeber, is implemented, which solved part of the tracking accuracy, however, the large position error still existed. Experiments are used to determine the nature of the tracking problem. Blade flapping and induced inflow generate drag forces acting on the quadrotor's in plane dynamics. Blade element theory and Momentum theory are used for inflow modeling, and blade flapping is modeled based on the work of Prouty. A thorough investigation is performed to investigate the limitations and modeling assumptions of Blade element theory, Momentum theory, and the blade flapping model. Furthermore, several flight cases of Blade element and momentum theory are combined to allow for three-dimensional trajectories. The blade flapping model of Prouty is adjusted to incorporate inflow coefficients and remove the assumptions of high speed forward flight. An extended model is developed to include those aerodynamics into the rigid body dynamics developed previously. This extended model has been implemented into a simulation environment, where it has been tested with three different cases, a three dimensional circular trajectory, a two dimensional circular trajectory, and a height varying trajectory. Compared to the experimental results the new model is capable of accurately estimating the z -dynamics, whereas the old model was not accurate enough. The performance in estimating the x and y -position in simulation has increased significantly compared to the simulation results of the old rigid body model, however, improvements are necessary. The simulation results of the new extended model are 50% more accurate compared to the experimental results than the old simulation results. The mismatch between the new simulation results and the experiments most probably is due to limitations in the blade flapping and inflow model. The inflow model does not capture the wake behavior under the rotors while it is known that these dynamics play an important role in the rotor dynamics, and consequently in the quadrotor dynamics. Furthermore, the inflow is based on a first order inflow variation, whereas higher order inflow variations are needed to fully describe the inflow behavior. Momentum and blade element theory are both static inflow models and are only valid in steady forward or axial flight and thereby neglecting the quadrotor's constant acceleration and deceleration necessary for trajectory following.

Contents

Abstract	III
Nomenclature	VII
1 Introduction	1
1.1 Background	1
1.2 Motivation and Objectives	2
1.3 Thesis outline	2
2 Problem identification	5
2.1 Quadrotor dynamics	5
2.2 Testbed	7
2.3 Experimental results	7
2.4 Additional experiments	9
2.5 Concluding remarks	14
3 Aerodynamic modeling of a UAV rotor system	15
3.1 Blade characteristics	15
3.2 Rotor configuration	18
3.3 Reference frames	19
3.4 Inflow	20
3.5 Rotor wake	21
3.6 Flapping behavior	23
3.7 Concluding remarks	25
4 Literature study	27
4.1 Rotor inflow and wake models	27
4.2 Blade flapping models	33
4.3 Concluding remarks	34
5 Theoretical model	35
5.1 Blade Forces	35
5.2 Inflow	42
5.3 Blade flapping	51
5.4 Extended model	56
5.5 Simulation results	58
5.6 Concluding remarks	61
6 Conclusions and Recommendations	63
6.1 Conclusions	63
6.2 Recommendations	64
Bibliography	67

Nomenclature

List of symbols

\mathbb{R}^n	The n-dimensional Euclidean space
$SO(n)$	The n-dimensional Special Orthogonal group
\mathcal{B}	Right-handed orthonormal body-fixed coordinate frame
\mathcal{C}	Right-handed orthonormal body-fixed wind axes coordinate frame
\mathcal{I}	Right-handed orthonormal inertial frame of reference
ψ_w	Angle between c_1 of \mathcal{C} and b_1 of \mathcal{B}
R_{bI}	Rotation matrix which transforms \mathcal{B} to \mathcal{I}
R_{cb}	Rotation matrix which transforms \mathcal{B} to \mathcal{C}
J	Inertia matrix
α_{bs}	Blade section angle of attack
α_d	Rotor disk angle of attack
γ	Blade lock number
θ_0	Rotor hub pitch angle
θ_{tw}	Rotor blade linear twist rate
σ	Rotor solidity
ϕ_{bs}	Blade section inflow angle
ψ_b	Rotor blade position
ω_n	Natural blade flapping frequency
Ω	Rotor angular velocity
a_0	Blade section two dimensional lift curve slope
A	Rrotor disk area
$c(r)$	The blade chord
C_{l_0}	Lift coefficient with zero angle of attack
e_f	Effective hinge offset
I_b	Moment of inertia of the blade about the center of rotation
$m(r)$	The blade mass
N	The number of blades
R	Rotor radius
C_d	Drag coefficient
C_l	Lift coefficient
C_H	Rotor drag force coefficient
C_T	Thrust coefficient
C_Y	Rotor side force coefficient

C_{M_x}	Roll moment coefficient
C_{M_y}	Pitch moment coefficient
H	Rotor drag force
M_x	Roll moment of single rotor
M_y	Pitch moment of single rotor
T	Thrust
Y	Rotor side force
K_c	Longitudinal inflow coefficient
K_s	Lateral inflow coefficient
L	Inflow gain matrix
M	Apparent mass matrix
S	Wake spacing
v_i	Rotor induced velocity
v_h	Rotor induced velocity in hover
V	Mass flow parameter matrix
V_c	Climb velocity
V_P	Perpendicular rotor blade velocity
V_r	Radial rotor blade velocity
V_T	Tangential rotor blade velocity
κ_c	Longitudinal wake curvature
κ_s	Lateral wake curvature
κ_T	Empirical hover thrust correction factor
λ_i	Rotor induced inflow ratio
λ	Total rotor inflow ratio
λ_0	uniform induced inflow
λ_c	side-to-side induced inflow variation
λ_s	fore-to-aft induced inflow variation
μ	Advance ratio
μ_c	Climb advance ratio
τ_D	Time constant matrix
χ	Rotor wake skew angle
β	Rotor blade flapping angle
β_{nc}	Rotor blade nth-order longitudinal flapping angle
β_{ns}	Rotor blade nth-order lateral flapping angle
ζ	Rotor blade lagging angle
ζ_{nc}	Rotor blade nth-order longitudinal lagging angle
ζ_{ns}	Rotor blade nth-order lateral lagging angle
θ	Rotor blade feathering angle
θ_{nc}	Rotor blade nth-order longitudinal feathering angle
θ_{ns}	Rotor blade nth-order lateral feathering angle
M_A	aerodynamic hinge moment
M_{CF}	Centrifugal hinge moment
M_w	Weight hinge moment

Acronyms

HP	Hub plane
CP	Control plane
NFP	No feathering plane
TPP	Tip path plane
MT	Momentum theory
BET	Blade element theory

Chapter 1

Introduction

1.1 Background

In the last decade the interest in Unmanned Aerial Vehicles (UAVs) has grown substantially. Even though UAVs have mainly been used for military applications, a considerable increase in interest for civilian and research applications is observed. One of the main advantages of UAVs is the possibility to automate several processes in a relative simple manner. For example, UAVs can be applied in agriculture, for automating tasks such as the dusting of crops and monitoring of livestock [1], assisting in rescue operations [2], wildfire detection, or emergency response. Lately, the trend in development of drone applications increasingly focuses on cooperation and formation flying, such as cooperatively carrying a payload [3]. In search and rescue missions a significant larger area can be searched when drones are capable of flying in formation. In the field of farming, such as dusting of crops, it would be an advantage if multiple drones can be deployed at the same time. Deploying multiple drones in a formation requires a tight formation and consequently collaboration between the drones.

In military applications the focus in UAV's is mostly on fixed wing UAV's. In commercial and research areas the focus is mainly on small, multi-rotor Unmanned Aerial Vehicles capable of vertical take off and landing (VTOL). The main advantages of these type of UAVs is their ability for vertical take off and landing, their high maneuverability, and ability to hover. Because of their simple geometry and fixed-pitch rotor designs they are mechanically simple and robust, which makes them economically interesting. From the multi-rotors the quadrotor is of particular interest, since it is the simplest configuration stabilizable for all six degrees of freedom by control of the four rotors. The system is unstable from nature due to its underactuation. Quadrotors have been the subject of a significant amount of studies concerning their dynamics and flight regulations, however, cooperation between drones is much less explored area.

This thesis is part of a larger research project, which strives to deploy a swarm of drones, capable of vertical take off and landing, in order to expand the applicability of drones. Deploying a swarm of drones or fly in formation requires close cooperation between the drones to avoid collision and perform their task accurately. Furthermore, as many applications will be in in the area of automation some level of autonomy is required. In this project the drones are required to perform a complete autonomous flight.

1.2 Motivation and Objectives

As already mentioned this thesis is part of a larger project on cooperation of drones. A major requirement in formations is collision avoidance, each drone needs to accurately hold its position in the formation. Because many application areas require some level of automation, the larger project specifies that the drones need to be able to fly completely autonomously.

In the larger project already some work has been done by [4] and [5], which were the first to work on this project. A sensor and actuator analysis is performed and an observer is designed by [4] to determine the position and orientation of the drone. Furthermore, a simulation environment for testing purposes and a graphical interface for communication with the drone were developed. In [5] a non-linear controller for autonomous trajectory tracking is developed together with a position and velocity observer. The combined result of [4] and [5] is a quadrotor capable of autonomously tracking a trajectory, however, for fast time-varying trajectories the tracking performance is insufficient. In a formation high accuracy trajectory tracking is of importance, therefore, adjustments to the previous work are required. The goal of this thesis is to improve the tracking performance by improving the quadrotor's dynamical model and perform a redesign of the controller to account for the new dynamics.

To achieve the main objective several sub-objectives can be distinguished

- Conduct experiments to determine the nature of the tracking problem,
- Study literature to obtain insight in the problem,
- Determine the current state in literature on quadrotor dynamic modeling,
- Make improvements to the rigid body model,
- Adjust the control to account for the new model,
- Validate the improvements.

These sub-objectives can be interpreted as an iterative process. From the results of the last sub-objective new problems might arise, or it might be concluded that the implemented adjustments are not sufficient enough.

1.3 Thesis outline

This thesis is organized as follows:

- **Chapter 2 Problem identification**

In this chapter the work of Jeurgens and van der Eijnden is closely examined. A short overview of their work is given, the rigid body model proposed for quadrotor control, the test environment, and the sensor data fusion. Furthermore, experiments are conducted to investigate the nature of the tracking problem.

- **Chapter 3 Aerodynamic modeling of a UAV rotor system**

Because in quadrotor literature not much information is found on aerodynamics of rotor systems, first a general elaboration on rotor systems, based on helicopter literature, is given. Furthermore, the interaction of the blade vorticity with the wake, and the wake influence regions are explained. Based on several common flight conditions the tendency of the rotor to flap up and down is described.

- **Chapter 4 Literature study**

In this chapter a literature study is performed to study the various methods and models to describe the inflow, wake, and blade flapping behavior.

- **Chapter 5 Theoretical model**

In this chapter the theory behind Blade element theory, Momentum theory, and blade flapping, is explained to create a deeper understanding of the fundamentals behind these theories. Furthermore, an extended model is proposed to incorporate these aerodynamics into the rigid body dynamics. The performance of the new quadrotor model is investigated and compared to the experimental results and the simulation results of Jeurgens and van der Eijnden.

- **Chapter 6 Conclusions and Recommendations**

The conclusions of this work and recommendations for future research are presented.

Chapter 2

Problem identification

This project is part of a larger research project, which strives to perform formation flying with quadrotors in order to expand the applicability of drones. In the larger project already some work has been done by [4] and [5] on implementation and trajectory tracking.

The work of [4] and [5] has resulted in a quadrotor capable of tracking a reference trajectory, although the performance is dissatisfactory. The work of [5] in modeling the quadrotor's behavior is summarized in section 2.1. The combined work, together with their experimental results is elaborated on in sections 2.2 and 2.3. Furthermore, additional experiments are performed using an improved controller to further investigate the nature of the tracking problem.

2.1 Quadrotor dynamics

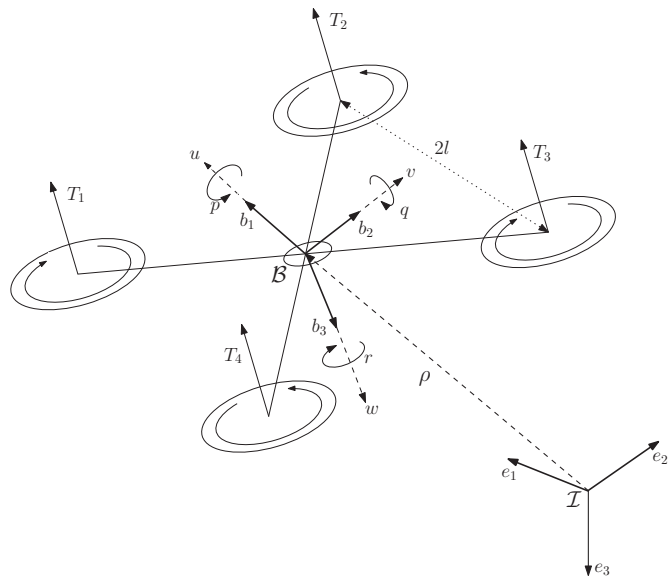


Figure 2.1: Schematic view of the quadrotor with Inertial frame \mathcal{I} and Body fixed frame \mathcal{B} .

The AR Drone is a quadrotor in x-configuration, the principal axis of the body frame are not aligned with the motor arms, see Figure 2.1. In modeling the simplified dynamics of the quadrotor, two right-handed orthonormal reference frames are introduced, an inertial reference frame \mathcal{I} with basis vectors $\{e_1, e_2, e_3\}$, and a body fixed frame \mathcal{B} with basis vectors $\{b_1, b_2, b_3\}$,

whose origin is aligned with the quadrotor's center of mass. In developing the simplified model of the quadrotor, the following assumptions are made:

Assumption 2.1.1. *Modeling assumptions:*

- (i) *The quadrotor is axis symmetric*
- (ii) *The quadrotor behaves as a rigid body*
- (iii) *The propellers are rigid*
- (iv) *The ground effect can be neglected*
- (v) *The aerodynamic forces can be neglected*

The first assumption aligns the geometric center of the quadrotor and its center of mass and the second assumption neglects bending in the quadrotor's structure. The third assumption rules out any bending of the rotors and implies that the rotor plane is always perpendicular to the b_3 axis of the body frame. The influence of ground effects become important near $z/r < 1$, where z is the height of the quadrotor and r the radius of the rotor [6]. In case of the AR Drone this is about a height of $z = 0.1[m]$. Therefore, the ground effect can be neglected during flight. The last assumption neglects possible existing aerodynamic drag forces.

The position of the center of mass of the quadrotor, with respect to the inertial frame, is given by $\rho = (x, y, z) \in \mathbb{R}^3$. The linear and angular velocities of the quadrotor, within the body frame, are defined as $\nu = (u, v, w)$ and $\omega = (p, q, r)$. The orientation of the body frame with respect to the inertial frame is represented by the rotation matrix $R \in \mathcal{SO}(3)$ with the special orthonormal group $\mathcal{SO}(3) = \{R \in \mathbb{R}^{3 \times 3} | R^T R = I, \det(R) = 1\}$. The orientation of the quadrotor, also called the attitude of the quadrotor, is parametrized by means of R , excluding singularities of Euler angles and the ambiguity of quaternions, [5, 7].

The quadrotor is controlled by the angular speeds of the four separate rotors. Each rotor produces a thrust and torque dependent on the angular speed of the rotor. A combination of these thrusts and torques generates the total thrust (f), the roll torque (τ_1), the pitch torque (τ_2) and the yaw torque (τ_3), such that holds

$$\begin{bmatrix} f \\ \tau_1 \\ \tau_2 \\ \tau_3 \end{bmatrix} = \begin{bmatrix} T_1 + T_2 + T_3 + T_4 \\ l(T_1 - T_2 - T_3 + T_4) \\ l(-T_1 - T_2 + T_3 + T_4) \\ d(T_1 - T_2 + T_3 - T_4) \end{bmatrix} \quad (2.1)$$

with d the drag constant of the blade and l the distance from the rotor to the axis of rotation [4].

Using Newton-Euler and the Poisson equation, the simplified dynamics of the quadrotor in the body frame are defined as [5]

$$\dot{\rho} = R\nu \quad (2.2a)$$

$$\dot{\nu} = -S(\omega)\nu + gR^T e_3 - \frac{f}{m}e_3 \quad (2.2b)$$

$$\dot{R} = RS(\omega) \quad (2.2c)$$

$$J\dot{\omega} = S(J\omega)\omega + \tau, \quad (2.2d)$$

with

$$J = \begin{bmatrix} J_{xx} & 0 & 0 \\ 0 & J_{yy} & 0 \\ 0 & 0 & J_{zz} \end{bmatrix},$$

and with $S(\omega)$ a skew symmetric matrix, such that any cross product can be written as $a \times b = S(a)b$:

$$S(\omega) = -S(\omega)^T = \begin{bmatrix} 0 & -\omega_3 & \omega_2 \\ \omega_3 & 0 & -\omega_1 \\ -\omega_2 & \omega_1 & 0 \end{bmatrix}. \quad (2.3)$$

2.2 Testbed

In [4] an actuator analysis is performed, in which the motor PWM commands are related to the generated thrust, torque, and rotor angular velocities. The results of this analysis are used to calculate the required thrust and torques for the motion controller designed in [5]. An observer, which consists of two linear Kalman filters, is designed to fuse the signals of several sensors of the internal measurement unit (IMU) and a top camera, to estimate the drone's position and orientation. The observer uses two linear Kalman filters in parallel are used to filter and fuse the signals. The implementation of these Kalman filters reduces the influence of noise and improves the accuracy. Furthermore, a supervisory controller is provided for controlling the drone at high level, allowing for sensor calibration, and safety precautions. Additionally, Jeurgens developed a simulation environment for testing purposes and a graphical interface for communication with the drone. The simulation environment contains the rigid body model to account for the quadrotor dynamics, his position observer, and the controller designed by van der Eijnden, including his velocity observer.

The position estimation of [4] is also based on position measurements of a top camera situated above the test area. This position measurement is developed by [8] and is based on a blob detection algorithm and capable of determining the drone's x, y coordinates and yaw angle. Because of the limitations of the AR Drone's processor the algorithm runs on a base laptop which receives the data from the camera, estimates the position and communicates this position with the drone via the wifi connection of the drone itself. A LED-strip is placed on top of the drone from which specific sequences of LED's can be on or off enabling identification of a specific drone and the drone's front.

Most developed control strategies are based on a linearization of the non-linear drone dynamics and use PID or LQR techniques to close loop stabilize the drone. Drawbacks of these strategies is that linearization limits the flight to small angle maneuvers and slow varying trajectories. To enable more aggressive maneuvering and track faster varying trajectories, [5] designed a cascade based controller based on non-linear PID control with conditional integrators. This controller requires both position and velocity measurements. However, the observer designed in [4] only determines the position and angles of the drone. Therefore, [5] implemented a position and velocity observer that estimates and filters the position and velocity of the AR Drone.

2.3 Experimental results

Both [4] and [5] performed experiments to test their implemented solutions and some of the results are discussed below. Figure 2.2 shows the results of the drone tracking a three dimensional circle, described by

$$\rho_r = [\cos(a_t t) \quad \sin(a_t t) \quad 1.5 + \sin(a_t t)]^T. \quad (2.4)$$

with a_t a time constant and $a_t = 1$. It can be seen that there is a difference in the desired trajectory, red, and the actual trajectory, black. The actual diameter, in the $x - y$ plane is about 1m, which is 50% of the reference diameter of 2m. Figure 2.3 shows the data of the 3D trajectory subdivided into each separate direction. In the representation of the y -displacement typical behavior is noticed in the sense that during descent the y -displacement remains more or less constant. This might suggest that in descent the quadrotor is affected by the turbulent air generated by the rotors. The behavior in the z -displacement looks to be damped compared to the desired altitude. In [4] the thrust of each rotor under hover conditions is derived. It might be the case that the varying airflow due to the three dimensional flight causes a reduction in thrust.

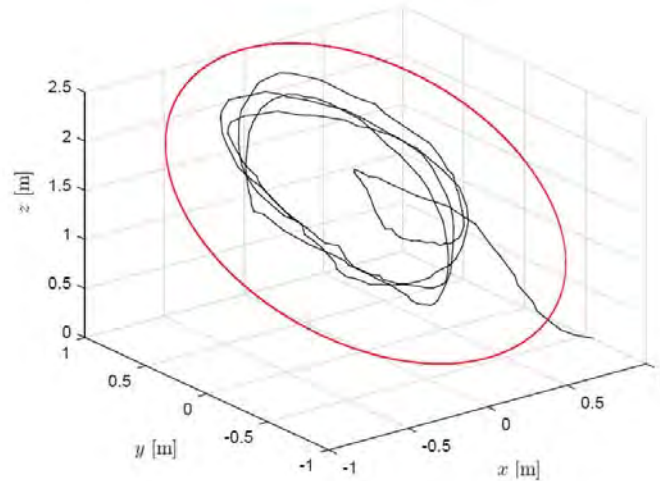


Figure 2.2: Spatial representation of the 3D trajectory for both the experimental results (black) and the reference trajectory (red) [5].

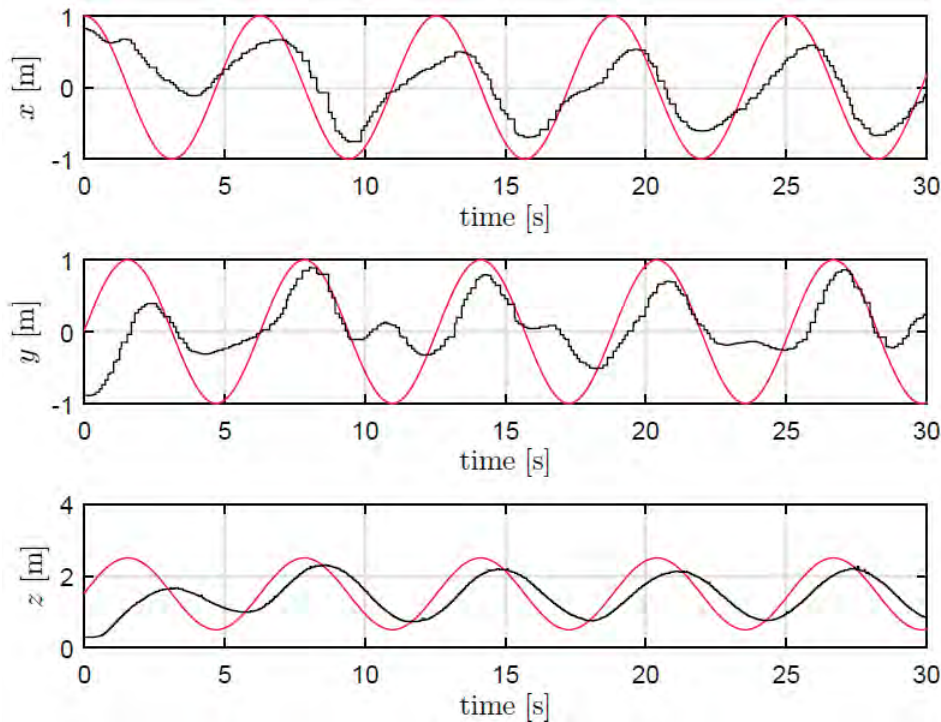


Figure 2.3: Representation of the 3D trajectory represented in each separate direction for both the experimental results (black) and the reference trajectory (red) [5].

Figure 2.4 shows the desired R_d (red) and actual $R_r^T \hat{R}$ (black) attitude split in terms of roll, pitch and yaw angles. The actual roll and pitch angles seem to be damped compared to the desired attitude. In the experiments the drone covers a smaller circle than the reference, which requires less aggressive angles. The yaw angle oscillates significantly more than desired and the peaks in the oscillation occur when the drone is almost at the top of the circle. At the top the linear velocity u is maximum and v is zero, after the top the velocity u decreases whereas v increases. This change in velocities might effect the desired attitude calculation which might cause the yaw oscillations.

Examining the results of the experiment more closely, it is noticed that the applied motor voltage does not exceed the maximum voltage limit, hence, the hardware is not the limitation. Furthermore, the experiments indicate that the controller is not capable of solving the permanent position error. Both observations suggest that unmodeled dynamics might be the underlying cause. Furthermore, it is important to note that

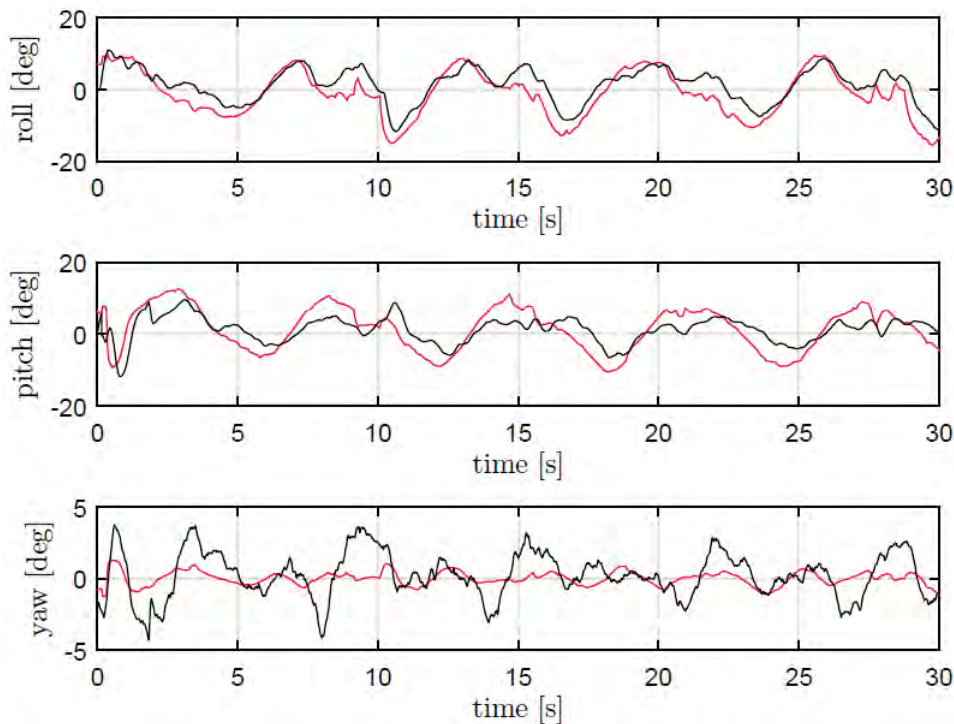


Figure 2.4: Estimated attitude $R_r^T \hat{R}$ (black) and desired attitude R_d (red) subdivided into roll, pitch, and yaw angles [5].

2.4 Additional experiments

The work of [5] is improved by [7] by redefining the desired attitude R_d . This improved controller is implemented on the AR Drone and additional experiments are conducted to create more insight in the tracking problem. Because in their experiments the y -direction has some strange behavior, two experiments are performed with in one experiment the x and y direction reversed, see figures 2.5 and 2.6. The trajectory in these figures is the same three dimensional trajectory as used in the experiments of [4] and [5], see Figure 2.3. Two observations can be made. First, no significant difference exists between the results of the two experiments. Secondly, compared to the experiment of [4] and [5] the typical behavior in y direction has disappeared. Presumably the improved controller is better capable of controlling the drone.

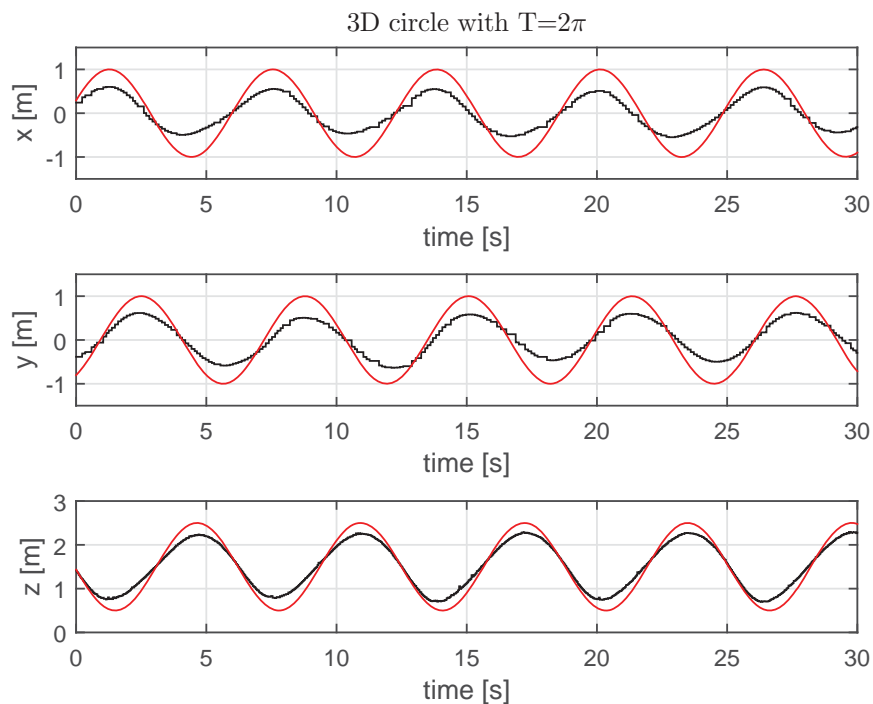


Figure 2.5: Representation of a 3D trajectory, equal to the trajectory of Figure 2.3, in each separate direction with the experimental results in black and the reference trajectory in red.

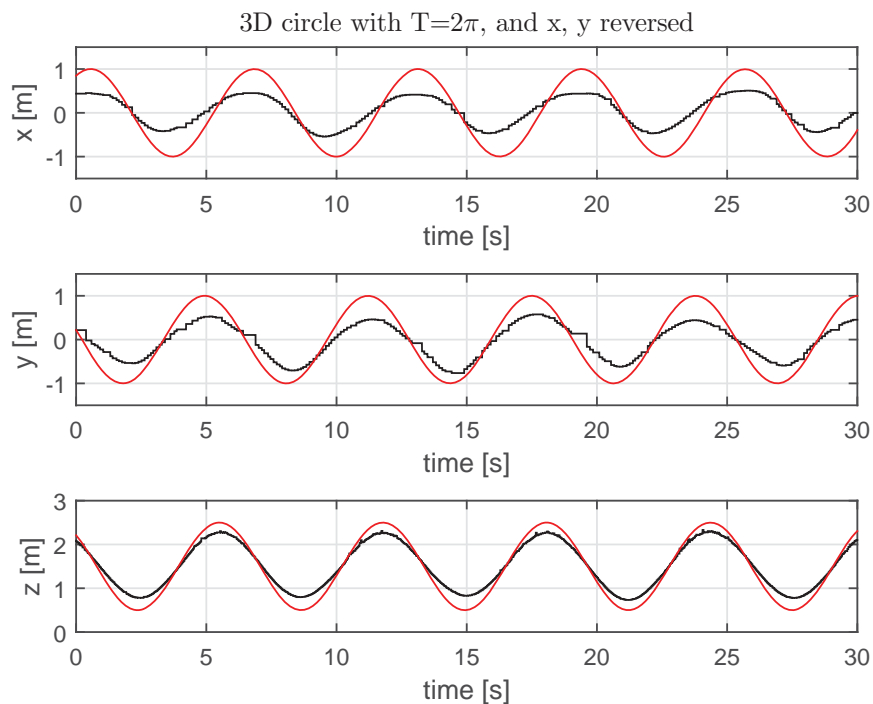


Figure 2.6: Representation of a 3D trajectory in each separate direction with the experimental results in black and the reference trajectory in red. The trajectory is equal to the trajectory of Figure 2.3, however, x and y are swapped.

Another problem observed in the test results of [4] and [5] is the reduced diameter in the $x - y$ plane. Two experiments are performed to investigate this behavior more closely, see figures 2.7 and 2.8. Figure 2.7 shows the same three dimensional trajectory as used in Figure 2.3, however, the period of the trajectory is ten times slower, i.e. $T = 20\pi$. The period of a reference trajectory can be determined by $T = 2\pi/a_t$, i.e. $a = 0.1$. As can be seen the drone is capable of tracking the slow time-varying trajectory, which could imply that the phenomena causing the diameter reduction are velocity dependent.

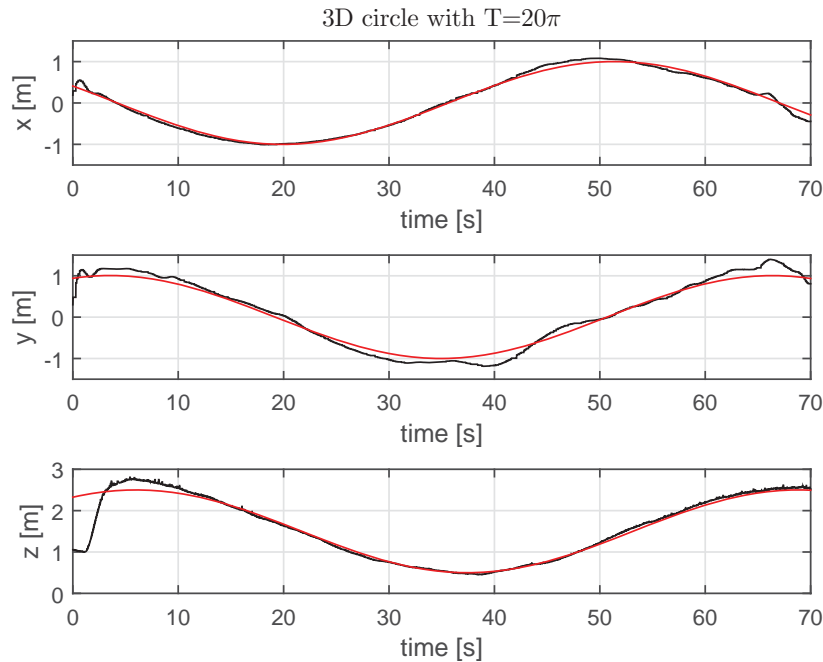


Figure 2.7: Representation of a 3D trajectory in each separate direction with the experimental results in black and the reference trajectory in red. The same trajectory is used as in Figure 2.5, however, the period is ten times slower, $T = 20\pi$.

Figure 2.8 shows the results of an experiment with a circle in the horizontal plane, parametrized as

$$\rho_r = [\cos(a_t t) \quad \sin(a_t t) \quad 1.0]^T. \quad (2.5)$$

with $a_t = 1$. The diameter of the reference equals two meters, whereas the actual performed circle only has a diameter of one meter. Compared to the three dimensional trajectory the x and y behavior is not significantly different, which might imply that the z -direction has no influence in the phenomena causing the reduced diameter.

A second set of experiments is conducted in which only z movement is allowed and the reference can be described as.

$$\rho_r = [0 \quad 0 \quad 1.5 + \sin(a_t t)]^T. \quad (2.6)$$

with a_t the time constant. Three different kinds of experiments are performed, in which the speed is adjusted. In the first experiment the period is $T = 10\pi$, i.e. $a_t = 0.2$, in the second experiment $T = 2\pi$, and in the third experiment $T = \pi$, see figures 2.9, 2.10, and 2.11. As in the case of the three dimensional trajectory, it can be seen that the quadrotor is capable of tracking a slow time-varying trajectory, however, when the speed increases the tracking performance decreases, see figures 2.9 and 2.10. Furthermore, shown in Figure 2.11 are the results of the experiment with $T = \pi$. The results show that the quadrotor is lacking behind in time and the amplitude is not constant anymore. From this it can be concluded that the rotors can not

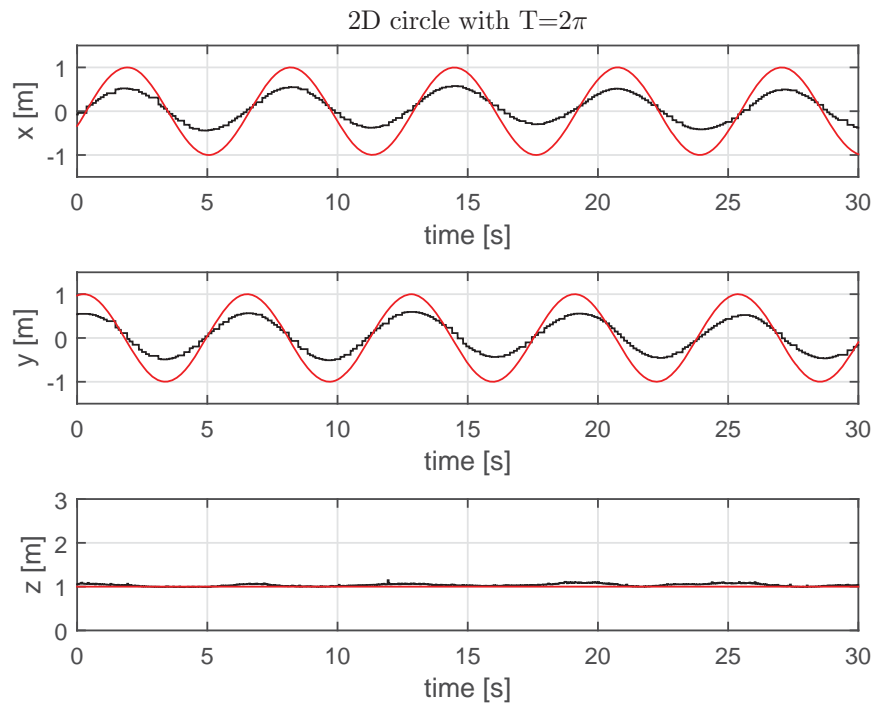


Figure 2.8: Representation of a 2D trajectory, with reference parameters $D_r = 2m$ and $T_r = 2\pi$. The experimental result is shown in black and the reference trajectory is shown in red.

deliver the thrust the fast varying trajectory demands, hence the limits of the quadrotor are reached.

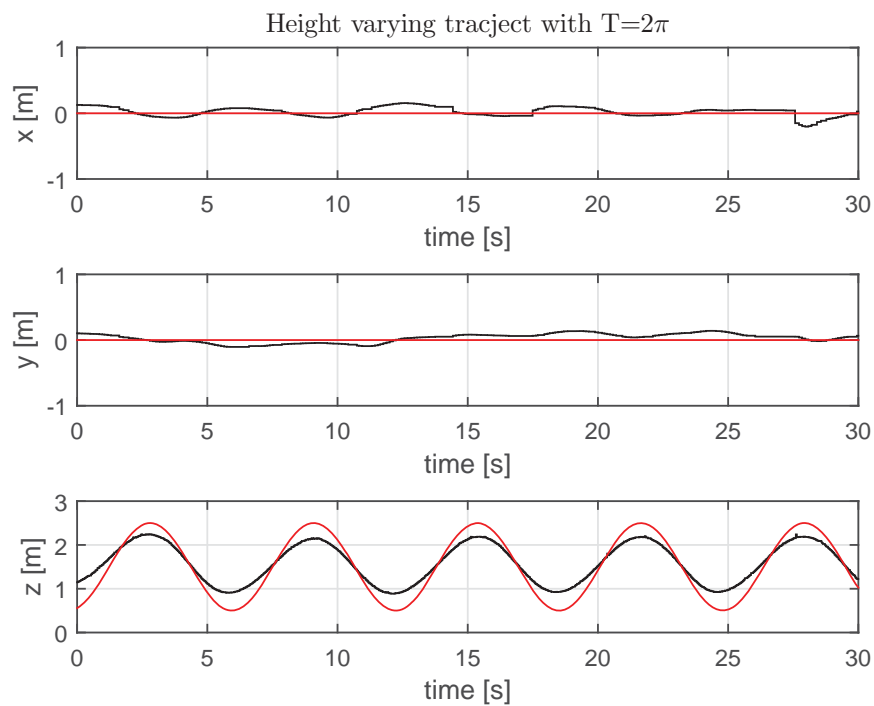


Figure 2.10: Representation of a height varying trajectory with $a_t = 1$, i.e. $T = 2\pi$.

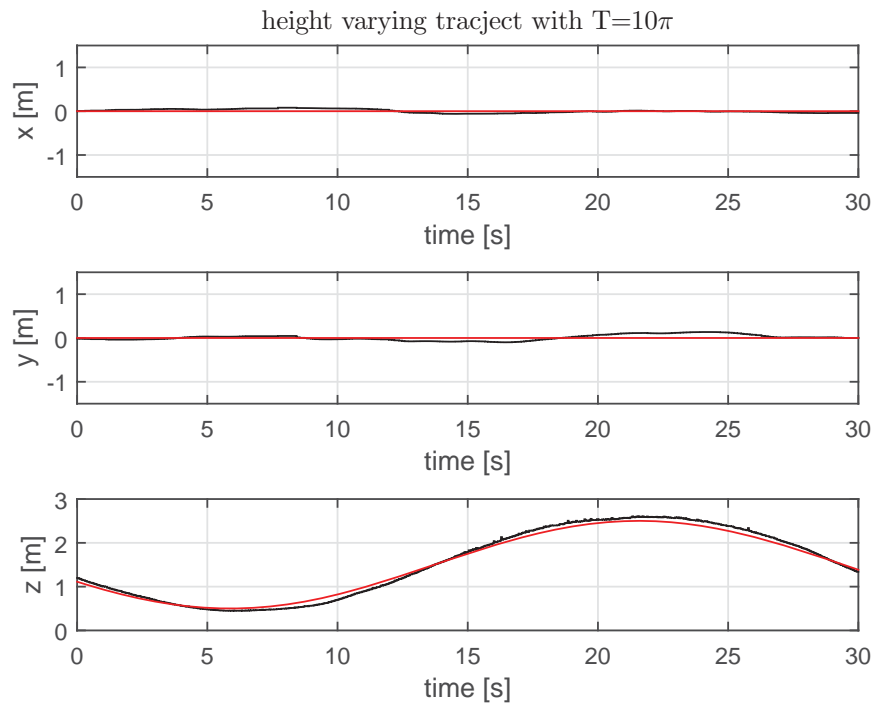


Figure 2.9: Representation of a height varying trajectory in each separate direction with the experimental results in black and the reference trajectory in red. The trajectory described in (2.6), with $a_t = 0.2$, i.e. $T = 10\pi$.

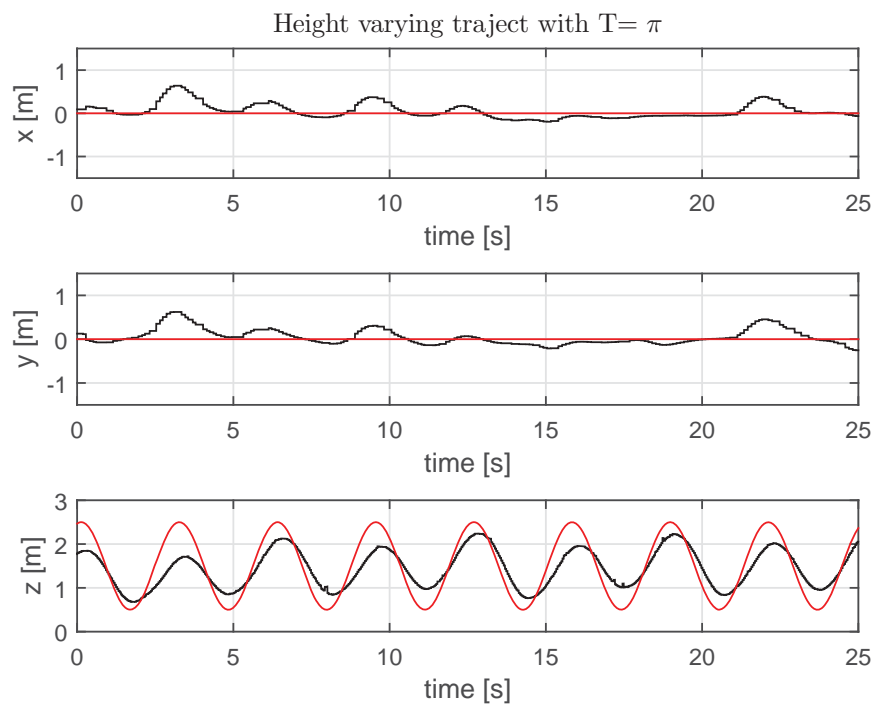


Figure 2.11: Representation of a height varying trajectory with $a_t = 2$, i.e. $T = \pi$.

2.5 Concluding remarks

Jeurgens [4] experimentally determined the thrust of each individual rotor for a given rpm or PWM value, however, these experiments were performed under hover conditions only. In order to avoid performing complex experiments and be able to switch to other drone platforms, without much effort, it would be of interest to determine the thrust analytically both in hover and forward flight.

The previous work performed by [4] and [5] resulted in a quadrotor capable of autonomous trajectory tracking, although the performance is not satisfactory. Based on the additional performed experiments it is suspected that the underlying modeling assumptions are causing this weak performance. In modeling the quadrotor's behavior aerodynamic interactions are neglected, see Assumption 2.1.1 (v). However, recent research, such as Bangura [9], and Omeri et al. [10], discovered that aerodynamics, such as induced inflow and blade flapping, influence the quadrotor's behavior. Both phenomena induce forces in the $b_1 - b_2$ plane of the quadrotor, the underactuated directions in the dynamics, and therefore cannot be easily counteracted by high gain control [11].

Mathematical models for predicting the flight behavior of a quadrotor are essential for the control design. The most basic quadrotor models, such as the model considered by [5], see section 2.1, are inadequate in predicting the quadrotor's behavior. An extended quadrotor model, which includes the rotor aerodynamics into the rigid body dynamics, is provided in Chapter 5. The next chapter establishes a basic knowledge about rotor aerodynamics to improve the reader's understanding and Chapter 4 elaborates on the different models for inflow, wake, and blade flapping behavior.

Chapter 3

Aerodynamic modeling of a UAV rotor system

In quadrotor literature not much information can be found on aerodynamics of rotor systems and the information presented in the quadrotor literature is always based on helicopter literature. Therefore, first a general elaboration on rotor systems, based on helicopter literature, is given to establish some basic backgrounds and explain some difference between the rotor system of a helicopter and that of the most quadrotors. Furthermore, the interaction of the blade vorticity with the wake, and the wake influence regions are explained. Based on several common flight conditions the tendency of the rotor to flap up and down is explained.

3.1 Blade characteristics

A rotor blade normally is twisted along its length. The twist of the rotor blade of the AR Drone is approximated with a linear variation, such that the blade pitch can be described as

$$\theta = \theta_0 + \Delta\theta = \theta_0 + \frac{r}{R}\theta_{tw}, \quad (3.1)$$

where θ_0 is the pitch angle at the rotor hub, r the radius to the section on the blade, and R the radius of the total rotor, see Figure 3.1.

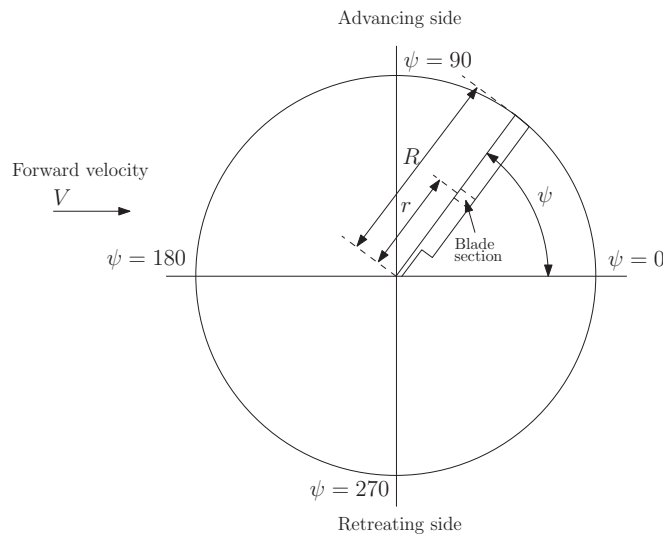


Figure 3.1: Rotor disk with the azimuth angle of a rotor blade, [12]

The linear twist rate θ_{tw} is equal to the tip pitch angle minus the root pitch angle and therefore negative. This approximation follows helicopter literature [12–14] and makes the derivations less complex, however, is not an optimal description of the rotor blade, since the blade near the blade root is more curved than near the blade tip, see Figure 3.2.



Figure 3.2: The rotor blade of the AR Drone 2.0

In rotor aerodynamics there are some important quantities, which are used very often

- The blade chord, $c(r)$
- The number of blades, N
- The blade mass, $m(r)$
- The moment of inertia of the blade about the center of rotation, I_b
- The rotor disk area, $A = \pi R^2$
- The rotor solidity, $\sigma = \frac{Nc}{\pi R}$
- The blade lock number, $\gamma = \frac{\rho acR^4}{I_b}$
- The blade section two dimensional lift curve slope, a_0
- The blade section angle of attack, α_{bs}
- The blade section inflow angle, ϕ_{bs}

The blade chord is the length of an imaginary straight line joining the leading and trailing edges of an airfoil. In general the chord length is a function of the rotor radius r , however, it is approximated by a constant equal to the average chord length. Furthermore, the blade mass depends on the rotor radius as well, however, it is assumed that the blades of the AR Drone have a uniform weight. The solidity, σ is the ratio of the total blade area, NcR , for constant chord, to the total disk area, A . The lock number, γ is the ratio between the aerodynamic forces and the inertial forces on a rotor blade.

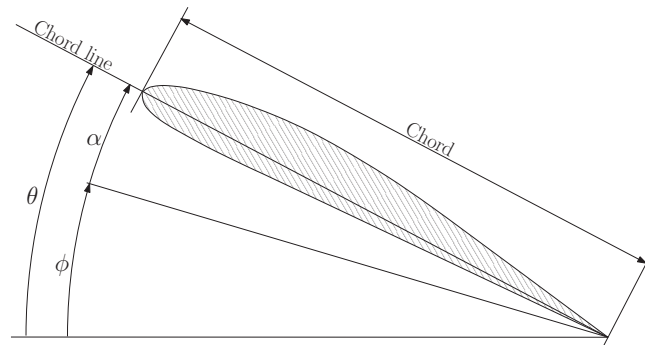


Figure 3.3: Blade section with the pitch angle θ and the chord of the blade section

Each blade section or airfoil can produce an amount of lift, which is represented by the lift coefficient C_l . This lift coefficient varies with the angle of attack of the blade section, α_{bs} . The slope of the curve of the lift coefficient against the angle of attack is called the lift curve slope a_0 , see Figure 3.4. When the angle of attack increases beyond the stall point, the air flow separates from the blade and stall occurs, resulting in less lift generation. Thin airfoil theory is a simple theory relating the angle of attack with the generated lift for incompressible frictionless flows. The theory neglects the stall region and assumes the flow around the blade section to be two dimensional, the blade section to be thin, and the blade to extend to infinity, which neglects tip vortices. Tip vortices affect the lift generation and therefore the lift curve slope. The lift curve outside the stall area can be represented by

$$C_l = a_0\alpha_{bs} + C_{l_0}, \quad (3.2)$$

where a_0 is the lift curve slope and C_{l_0} the lift generated with $\alpha_{bs} = 0$. The theoretical value of the lift curve slope equals, $a_0 = 2\pi$. In quadrotor literature a value around 5.7 is proposed [15,16], to incorporate the effect of tip vortices.

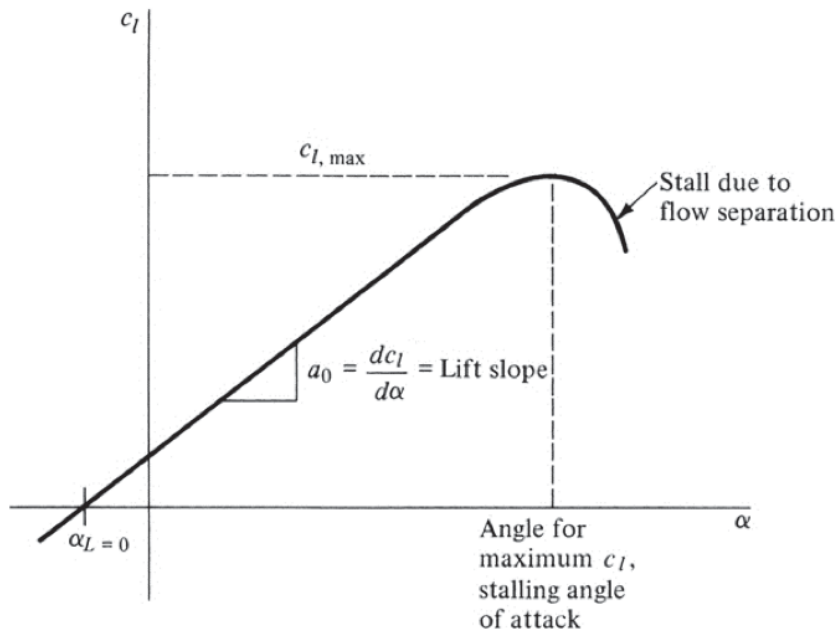


Figure 3.4: The lift curve of an arbitrary airfoil, with the lift slope curve a_0 [17]

The position of a rotor blade relative to the free stream velocity is represented by the azimuth angle, ψ_b , which is defined zero at the downstream direction, see Figure 3.1. In most helicopters the rotor angular velocity is constant and the pitch angle of the blades can be adjusted to generate more or less thrust, known as collective and cyclic pitch control. Because of the constant rotor angular velocity the azimuth angle of a helicopter rotor blade can be defined as $\psi_b = \Omega t$. The hingeless rotor of a quadrotor does not possess collective and cyclic pitch control and therefore the amount of thrust generated is influenced by increasing or decreasing the rotor angular velocity. Since the rotor velocity is not constant the azimuth can be defined as

$$\psi_b = \int_0^t \Omega dt + C, \quad (3.3)$$

however, this is true for any constant C , which is difficult to determine.

3.2 Rotor configuration

A helicopter rotor is hinged at the blade root to relieve the blade root of large bending stresses and eliminate the rolling moment arising in forward flight, see Section 3.6. The blade has three hinges to allow the blade to flap up and down (flapping), to move back and forth, (lead-lag) and to pitch up and down (feathering).

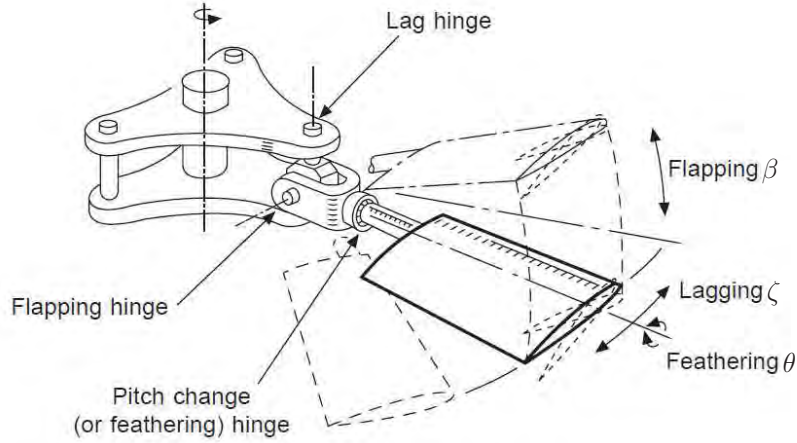


Figure 3.5: Rotor hinge system with flap, lag, and feathering hinges, [18]

Blade flapping hinges allow the blade to move up and down relative to the hub plane under influence of the surrounding air. Due to the forward speed of the helicopter a lift difference arises between the different rotor blades. Because of this difference each blade flaps up or down, see Section 3.6 and the angle between the blade and the disk plane is described by the flap angle, β . A consequence of blade flapping is lead-lag movement. As a blade moves up or down the radius of the orbit described by the blade tips increases or decreases. Therefore, due to the Coriolis effect the rotor blade wants to speed up or down and thereby lead or lag from their initial position. The angle between the blade and its normal position is given by the lead-lag angle, ζ . The feathering hinge allows the blades to rotate lengthwise and thereby increases or decreases the pitch angle. The pitch angle, θ , influences the amount of lift generated and is influenced in helicopters by the pilot controls.

In steady state the motion of the rotor is periodic and therefore the blade angles can be approximated by a Fourier series

$$\begin{aligned}\beta &= \beta_0 + \beta_{1_s} \sin(\psi) + \beta_{1_c} \cos(\psi) + \dots + \beta_{n_s} \sin(n\psi) + \beta_{n_c} \cos(n\psi) \\ \zeta &= \zeta_0 + \zeta_{1_s} \sin(\psi) + \zeta_{1_c} \cos(\psi) + \dots + \zeta_{n_s} \sin(n\psi) + \zeta_{n_c} \cos(n\psi) \\ \theta &= \theta_0 + \theta_{1_s} \sin(\psi) + \theta_{1_c} \cos(\psi) + \dots + \theta_{n_s} \sin(n\psi) + \theta_{n_c} \cos(n\psi).\end{aligned}\tag{3.4}$$

Most multirotor UAVs contain hingeless fixed rotors, which means that the blades are cantilevered restrained to the rotor hub. Due to the flexibility of the blades they possess the flapping characteristics but lag the lead-lag and feathering motions. However, in practice the hingeless rotor of the AR Drone experiences all three phenomena of which blade flapping is of most influence and the most common topic in recent research.

Helicopter literature often rewrites a variable into its corresponding coefficient form. A few important coefficients are

- The lift coefficient, $C_l(\alpha_{bs})$
- The drag coefficient, $C_d(\alpha_{bs})$
- The thrust coefficient, $C_T = \frac{T}{\rho A (\Omega R)^2}$
- The rotor drag force coefficient, $C_H = \frac{H}{\rho A (\Omega R)^2}$
- The rotor side force coefficient, $C_Y = \frac{Y}{\rho A (\Omega R)^2}$
- The pitch moment coefficient, $C_{M_y} = \frac{M_y}{\rho A R (\Omega R)^2}$
- The roll moment coefficient, $C_{M_x} = \frac{M_x}{\rho A R (\Omega R)^2}$,

where H is the rotor drag force and Y the rotor side force, which depend on the lift and drag force generated by the blades, see Figure 3.6. The lift and drag coefficient depend on the angle of attack of the blade section α_{bs} . The thrust coefficient is equal to the thrust T divided by the air density ρ , the area swept out by the rotor blades A , the angular velocity of the rotor Ω and the rotor radius R . The pitch moment M_y and roll moment M_x are divided through R^3 to derive the pitch and roll moment coefficients instead of R^2 as is the case with the force coefficients.

To describe the behavior of the rotor blades and their interaction with the body, helicopter literature defines four different planes, namely

- The hub plane, HP
- The control plane, CP
- The no feathering plane, NFP
- The tip path plane, TPP

The plane perpendicular to the rotor shaft, and therefore parallel with the plane spanned by b_1 and b_2 , see Chapter 2, is called the hub plane. With help of the swashplate the cyclic pitch input is altered and this pitch input defines the control plane. The no feathering plane describes the plane in which the pitch angle is constant. Since the rotor of the AR Drone does not contain a swashplate, and collective and cyclic pitch control, and in this report only blade flapping is considered, the hub plane, control plane, and no feathering plane align with each other. The tip path plane is the plane described by the motion of the tips of the blade.

3.3 Reference frames

In the previous chapter an inertial frame, \mathcal{I} , and body frame, \mathcal{B} , have been introduced to describe the quadrotor's position, translational and angular velocities. For modeling purposes an additional frame is introduced, a body fixed wind axis frame \mathcal{C} with basis vectors $\{c_1, c_2, c_3\}$. The origin of the \mathcal{C} frame is aligned with the origin of the body frame \mathcal{B} and the c_3 axis is aligned with the b_3 axis. The difference between the two body fixed frames is the orientation of the c_1 axis, where b_1 is fixed the c_1 axis is always aligned with the flight direction and positive pointing forward. The c_2 axis completes a right hand frame. The mapping from frame \mathcal{C} to frame \mathcal{B} can be performed using the Rotation matrix R_{cb} and is defined by

$$R_{cb} = \begin{bmatrix} \cos(\psi_w) & -\sin(\psi_w) & 0 \\ \sin(\psi_w) & \cos(\psi_w) & 0 \\ 0 & 0 & 1 \end{bmatrix}, \quad (3.5)$$

where ψ_w describes the angle between the c_1 and b_1 axis.

3.4 Inflow

For a quadrotor to perform a level forward flight it must pitch or roll around its body axis which results in an angle of attack of the rotor disk, α_d . A rotor in forward flight experiences an incoming velocity equal to the quadrotor's forward velocity corrected for the angle of attack. Furthermore, it is common to normalize the velocities by dividing through the blade tip speed. The normalized forward velocity is called the advance ratio, μ and is defined as:

$$\mu = \frac{V \cos(\alpha_d)}{\Omega R}. \quad (3.6)$$

A rotor produces thrust by influencing the environmental air. The air above the rotor is sucked in and accelerated as it passes through the rotor, this phenomenon is called induced velocity, v_i . Normalizing the induced velocity results in the induced inflow ratio λ_i . Adding the vertical component of the forward flight velocity and normalizing with the tip speed results in the rotor inflow ratio, λ :

$$\lambda = \frac{V \sin(\alpha_d) + v_i}{\Omega R} = \mu \tan(\alpha_d) + \lambda_i. \quad (3.7)$$

The induced velocity and therefore also the induced inflow is defined to be normal to the disk plane, see Figure 3.6.

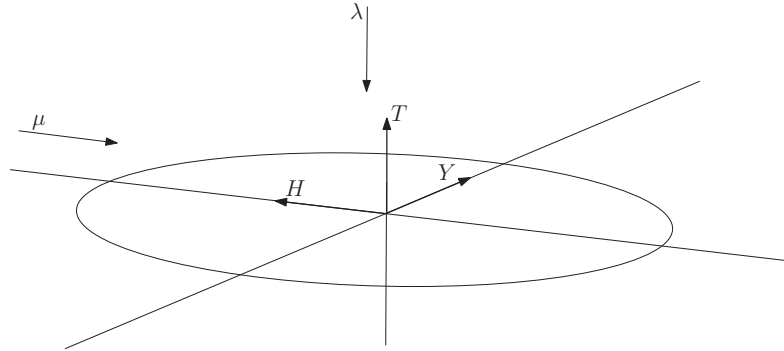


Figure 3.6: Rotor disk with the induced velocity and advance ratio and the rotor hub forces T, H, Y , [12]

The rotor creates both an inflow and outflow, called the wake. In vertical climb and hover it can be assumed that the inflow and outflow are along streamlines and therefore can be estimated using blade element theory and momentum theory, see Chapter 5. In descent, however, the rotor passes through its own wake, which in slower rates of descent is turbulent, see Figure 3.7.

Based on the work of Prouty [14] two descent regions can be distinguished: the vortex ring state, and the Windmill brake state. In literature for comparison reasons it is common to normalize the descent velocity V_c with the induced velocity during hover v_h . In very low rate of descent, meaning that the rate of descent is smaller than approximately a quarter of the hover induced velocity, $V_c/v_h \leq 1/4$ [14], and high rate of descent, $V_c/v_h \geq 2$, the flow through the rotor can be assumed to be along streamlines. Note that in high rates of descent the rotor wake is above the rotor instead of below as in hover and climb.

A rotor operates in the vortex ring state when descending at low forward speed with a vertical velocity larger than, $V_c/v_h \geq 1/4$ and below $V_c/v_h \leq 2$. In this condition the rotor tip vortices are not convected away from the disk rapidly enough. The tip vortices collect in a vortex ring, producing a circulating flow down through the rotor disk, then outward, upward outside the disk and back through the rotor, as shown in Figure 3.7, and the main flow through the rotor

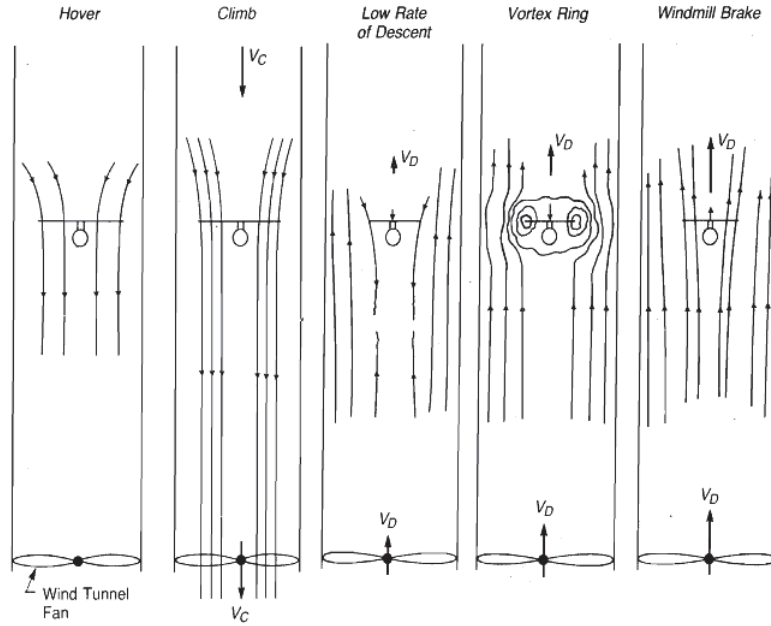


Figure 3.7: Vertical flight flow state illustrated by wind tunnel conditions [14]

is downward. With each rotor revolution the ring vortex builds up in strength until it breaks away from the disk plane in a sudden breakdown of the flow. The resulting flow is unsteady, hence a source of considerable low frequency vibrations and possible control problems [12, 14]. For descent at forward speeds sufficiently high the wake is convected away from the rotor and the vortex ring state does not arise.

Johnson and Leishman [12, 13] divide the vortex ring state into two regions, the vortex ring state and the Turbulent wake state with the boundary at $-V_c + v_i = 0$. In contrast to the vortex ring state, in the turbulent wake state the main flow through the rotor is upward. As in the vortex ring state the tip vortices produce a recirculating flow, however, in the turbulent wake state the recirculating flow is just above the rotor disk instead of at the rotor disk. The rotor, therefore, still experiences vibrations due to turbulence but not as significant as in the vortex ring state [12]. No clear distinction exists between the vortex and turbulent wake state. As the descent velocity approaches the boundary of the windmill brake state, $V_c/v_h \geq 2$, the flow gradually turns from the vortex state into the turbulent state.

In the Windmill brake state the rate of descend is sufficiently high, i.e. $V_c/v_h \geq 2$, and the far downstream wake is above the rotor disk. In this state the flow can be assumed to flow along streamlines and the same conditions can be applied as in the climb and low rate of descent case.

3.5 Rotor wake

In general a rotor wake is a very complex structure which can vary its behavior in time from what could be observed as chaotic to a wake in which some patterns can be distinguished. The first in-depth flow visualisation study of the wake of a rotor in forward flight and hover was performed by Gray [19, 20]. In his flow visualization studies he used smoke to visualize the wake behavior. Based on his data the vortex model for a single-bladed rotor in hover, as shown in Figure 3.8, was developed. It was discovered by Leishman [21] that in hover and low-speed maneuvers the rotor wake geometry is inherent unstable

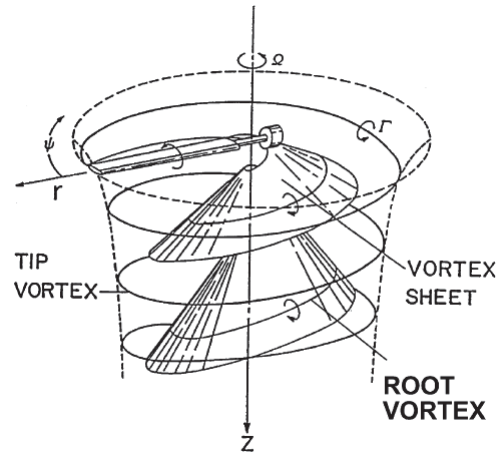


Figure 3.8: Geometry of the wake of a single-bladed hovering rotor determined using the flow visualisation studies of Gray [20]

Observed from the data three main components influence the wake: the blade tip vortex, vortex inboard sheet and root vortex. Furthermore, the influence of the wake on the rotor can be divided into three regions near, mid and far wake. These three regions are not formally defined but are defined from a practical point of view. The classification is based on the influence of the region on the rotor and body.

3.5.1 Blade vorticity

For a rotor the largest velocity is achieved near the tip of the blades, consequently it is the most aerodynamically loaded part of the rotor with the most influence on the rotor behavior. Tip vortices are high strength vortex filaments, i.e. thin segments, arising from sudden changes in circulation near the blade tip and follow a helical path down into the wake. Although the tips are the most influential part of the blade, the tip vortex geometry is shown to be independent of tip speed [22]. Some models cope with the tip vortices by including a tip loss factor and was first introduced by Glauert [23]. Mostly tip vortices are modeled as filaments on the outer line of the wake following the rotational flow field along the near and mid wake. In the far wake the tip vortices evolve into two counter-rotating vortices [24, 25].

Inboard vortex sheets can be described as continuous thin sheets shed from the inboard or trailing edge of the blade. The assumption of the inboard vortex sheet being confined to a thin sheet is only valid under the assumption of high Reynolds number [26]. The vortex sheets contain several vortex filaments confined to very thin regions which are surrounded by substantially irrotational fluid and the direction of circulation of the inboard sheet is opposite to that of the tip vortices [27]. The vortex sheets are of high influence in the vicinity of the rotors, i.e. in the near wake, and effect both inflow and blade loading. Although the axial velocity of the outer end of the vortex sheet is greater than that of the tip vortex it is assumed that the inboard sheet retains some connection with the tip vortex [22]. The simplest way of modeling the inboard sheet is using a collection of straight line segments, as depicted in Figure 3.9. This modeling uses the vortex box elements, introduced by Egolf [28], which consist of four, straight, constant strength vortex segments combined to form a wake structure.

The root vortices are similar to the tip vortices, however, they are of lower strength and caused by the rotor hub. The behavior of the root vortices are similar to the tip vortices. However, in contrast to the tip vortices which evolve into two counter-rotating vortices, root vortices exist in all the three main wake regions [25].

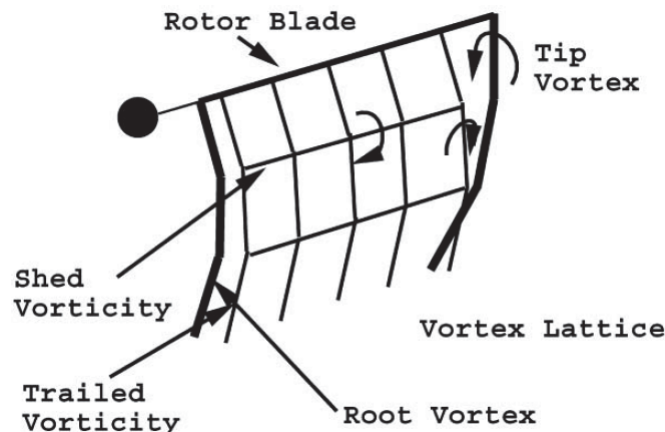


Figure 3.9: The inboard sheet as a collection of vortex boxes modeled by straight line segments [28]

3.5.2 Wake regions

The near wake is considered the closest region to the blade where the vortical elements are released from the blade into the wake. This region is of high importance because of its influence on the blade airloads and dynamics, and on the inflow behavior. The near wake covers a region within approximately two rotor revolutions, within those two revolutions the rotor wake fully develops and complete wake contraction takes place [24, 25].

The mid wake is the region in which the wake interacts with the aircraft's body, such as the fuselage. In case of helicopters this region is of importance because of the rotor-fuselage interaction. In quadrotors, however, the main part of the fuselage is located outside the rotor wakes and therefore the mid wake is not as important as with helicopters.

In the region beyond the body of the craft, the far wake, the wake still influences the velocity distribution over the rotor and consequently the rotor behavior and flight dynamics. The far wake includes the regions where wake environment interaction, such as ground effect, sling loads, and formation flying are important. Furthermore, in case of the quadrotor, rotor wake interference is of importance.

3.6 Flapping behavior

Blade flapping hinges are incorporated in helicopter rotors to alleviate the stresses at the connection of the hub and the blade. Furthermore, the capability of the blade to flap up and down positively influences the stability of the rotor itself, and thereby influencing the helicopter behavior. In helicopters blade flapping is included in the pilots control and can be compensated for. In quadrotors, however, this control is not available due to their rigid attachment and therefore the blade flapping forces act as drag forces in the $b_1 - b_2$ plane of the body frame. To understand the behavior of blade flapping some most common blade flapping characteristics are more thoroughly analyzed.

Change in forward speed is of most influence on the characteristics of blade flapping. In translational flight, the advancing blade of a rotor experiences a higher effective velocity relative to the air, creating an increase in lift, while the retreating blade experiences a lower effective velocity and therefore a reduction in lift, see Figure 3.10. While the advancing blade accelerates

up it is rotated towards the nose, reaching its maximum upward angle and decreasing its angle of attack. The retreating blade experiences the opposite and reaches its maximum downward angle at the tail and increases its angle of attack. Equilibrium is reached when the flapping velocities of the blades are just enough to change the angles of attack to compensate for the change in lift. Implying that the flapping increases as the quadrotor's speed increases.

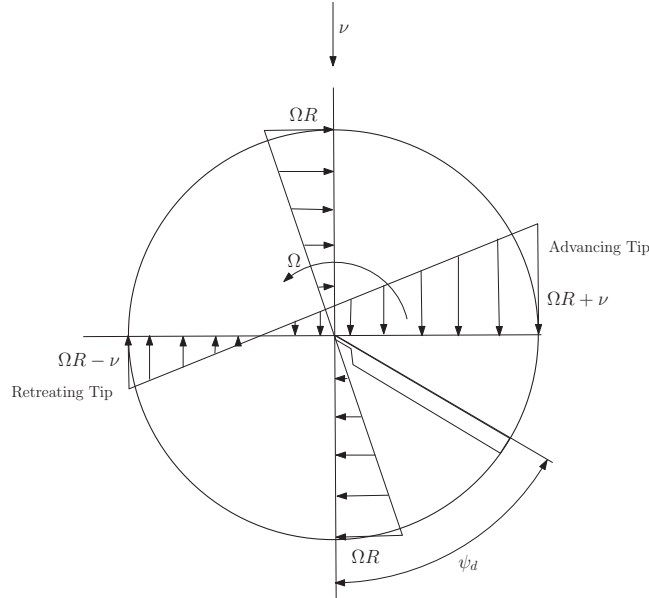


Figure 3.10: Schematic representation of the velocities acting on a rotor [14]

The blade flapping angles cause the tip path plane (TPP) to tilt backwards. Since the thrust is always perpendicular to the TPP the thrust vector is tilted rearwards, see Figure 3.11, inducing a pitching up moment and drag force on the rotor hub. The change in longitudinal flapping with increased speed is therefore stabilizing since the upward tilt of the TPP causes a rearward tilt of the thrust vector which slows down the quadrotor [14].

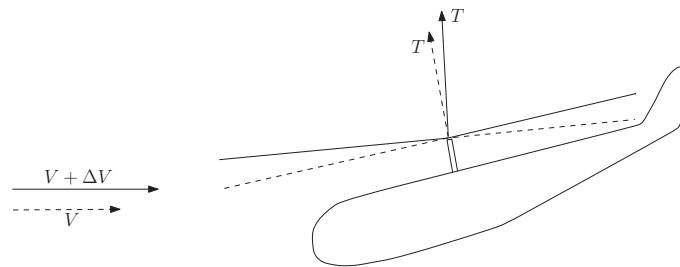


Figure 3.11: Schematic representation of nose up pitching moment due to increasing speed [14]

Lateral flapping in forward flight is, just as longitudinal flapping, caused by asymmetric airloads. In lateral flapping the difference in airloads is at $\psi = 0^\circ$ and $\psi = 180^\circ$ and is caused by coning. Coning causes the blades to tend upwards and form a cone. In forward flight the blade over the nose is affected by a more upward velocity component than the blade over the tail. This asymmetry in vertical velocity results in an asymmetrical angle of attack. The maximum response is 90° later and thus lateral flapping that is upward on the retreating side [14].

When the shaft of a helicopter is pitched during hovering, aerodynamic forces force the tip path plane to align itself perpendicular to the shaft [14]. The rotor disc acts as a gyroscope and remains in its original plane, at first, while the shaft is already tilted away from vertical. The

pitch angle is measured from the shaft, therefore, the angle of attack of the advancing blade is increased and that of the retreating blade is decreased. These changes result in a flapping rotor until equilibrium is reached, when the rotor is perpendicular to the shaft and the moments are balanced. For a rotor in hover with constant mass distribution it can be derived [14]

$$\frac{\omega_n}{\Omega} = \sqrt{1 + \frac{\frac{3e_f}{2R}}{1 - \frac{e_f}{R}}}, \quad (3.8)$$

with ω_n the natural frequency of the blade flapping, Ω the rotor speed, e_f the effective hinge offset, and R the rotor radius. Applying the parameters of the AR Drone rotor results in a value of $\omega_n/\Omega = 1.17$. This is within the bounds for cantilevered rotors found in literature and shows that the blade flapping frequency is faster than the rotational frequency of the blades, i.e. the flapping behavior is within one rotor revolution.

3.7 Concluding remarks

To establish a basic understanding of rotor configurations and dynamics, a general elaboration on rotor systems has been given. Moreover, the difference between a helicopter rotor and most quadrotor rotors has been explained. Several parameters necessary for modeling the blade forces and inflow have been derived. The inflow and wake behavior influence the behavior of the quadrotor through the rotors, especially in the vortex ring state where the surrounding air is turbulent. This influence is of importance in estimating the quadrotor's behavior. Furthermore, blade flapping introduces drag forces and moments which counteract the forces and moments necessary for following the trajectory. Both phenomena are thus important aspects which need to be accounted for in the quadrotor model. With the acquired knowledge the reader can distinguish the different phenomena in the inflow and wake and possesses insight in the subject to understand which phenomena are important to account for in modeling the quadrotor. In the next chapter the different methods and models to describe inflow and wake, and blade flapping behavior are investigated.

Chapter 4

Literature study

In Chapter 2, the inaccurate tracking performance has been investigated using experiments. Based on recent studies, rotor aerodynamics, such as inflow and blade flapping, are suspected of causing this poor performance. In the previous chapter a basic understanding of rotor systems and aerodynamics has been developed. In this chapter a literature study is performed to study the various methods and models to describe the inflow, wake, and blade flapping behavior.

4.1 Rotor inflow and wake models

Various methods and models have been developed to describe inflow and rotor wake behavior making use of a wide range of fundamental solutions. A general classification can be made based on the modeling approaches. The inflow models, which only model the velocity distribution at the rotor disk, and the wake models, which capture the dynamics of the entire wake. Figure 4.1 gives an overview of the inflow and wake models and their subdivisions.

The inflow models can be subdivided into two categories, the static and dynamic inflow models. An extensive review of the static inflow models under different flight conditions can be found in [29] and a detailed overview of the dynamic inflow models is given in [30]. The main difference between static and dynamic inflow is that static inflow models assume the induced velocity to build up instantaneously, in response to changes in disc-loading or aerodynamic moments, whereas dynamic models incorporate the effect of such rotor behavior in a dynamical fashion [29, 31].

The wake models can roughly be subdivided into two categories, the vortex methods and the computational fluid dynamics (CFD) methods. The vortex methods use the Biot-Savart law to evaluate the induced flow at a point located in the vortex tube. Several approximations have been made to the vortex method to simplify the equations and reduce the computation time. The vortex methods can be classified into three categories: rigid, prescribed, and free wake models, from which the free wake models are the most advanced and best in capturing the wake behavior. The most advanced wake models use CFD to solve the Navier-Stokes equations describing the wake behavior. However, the Navier-Stokes equations are difficult to solve and are computationally expensive, which led to the development of various approximations to derive simpler solutions. Based on the work of [27] a subdivision can be made, see Figure 4.1.

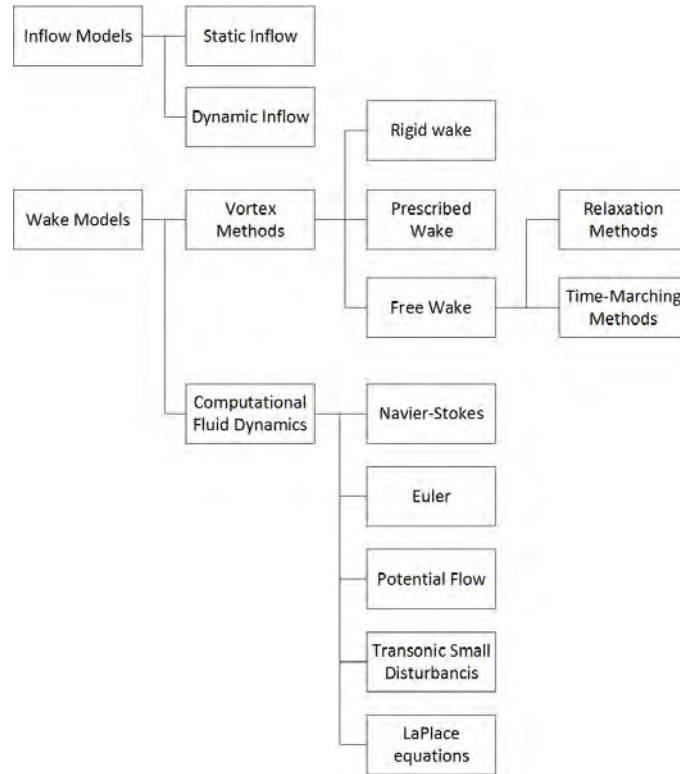


Figure 4.1: Overview of the inflow and wake models

4.1.1 Static inflow models

Momentum theory [32] is developed by Glauert and is the most common and widely used model of the static inflow models and is the basic model on which most other models are based. Momentum theory is based on Glauert's hypothesis of uniform inflow through the rotor disk and considers a rotor as an actuator disc, a circular surface with zero thickness which can support a pressure difference, with the accelerating air forming a stream tube, see Figure 5.4. The three energy conservation laws, conservation of mass, energy, and momentum, are used to relate the induced velocity at the rotor disk to the thrust generated by the rotor disk. Note that the conservation laws are derived with respect to an inertial reference frame and therefore only hold in hover and steady axial or forward flight. The uniform inflow assumption may be reasonably valid in hover and axial flight, however, it fails in forward flight where most of the wake is located below the rear half of the rotor [31]. Glauert acknowledges this fact when he observed discrepancies between the experimentally and theoretically calculated forces on the rotor using uniform inflow. In trying to resolve this problem he proposed a first harmonic non-uniform inflow distribution [32]

$$v = v_i \left(1 + K_c \frac{r}{R} \cos(\psi) \right), \quad (4.1)$$

where K_c is the longitudinal inflow coefficient. In [32] K_c is left unspecified, however, research has been performed to establish a relation for K_c . The tip vortices, which describe a helical profile, are approximated by a series of circular rings with constant vortex strength [33]. Biot-Savart's law and numerical integration are used to compute the induced velocity at the rotor disk [31]. The numerical integrals are replaced with analytical integrals and the rings with a skewed continuous sheet of vorticity by [31, 34]. It is shown by [34] that the induced velocity at the rotor disk strongly depends on the wake skew angle χ

$$\chi = \frac{\mu}{\lambda}. \quad (4.2)$$

An approximation of the results of [34] is suggested [29]

$$v = v_i \left(1 + K_c \frac{r}{R} \cos(\psi) + K_s \frac{r}{R} \sin(\psi) \right), \quad (4.3)$$

with K_s the lateral inflow coefficient. Dependency of the induced velocity on the wake skew angle is shown by [34]. Furthermore, the inflow coefficients depend on the advance ratio because they must equal zero in hover, where uniform inflow can be assumed. Cheeseman and Haddow obtained induced velocity data from a wind tunnel test and compared the different definitions of the longitudinal K_c and lateral K_s inflow coefficients with their data and concluded that the model of Pitt/Peters and Drees compared best. For a detailed survey on the static non-uniform inflow models see [29].

The actuator disk model, which is a fundamental assumption in momentum theory, represents a rotor with an infinite number of blades, therefore, the detailed flow is different from a real rotor with a small number of blades. Furthermore, in lower rates of descent the tip vortices are pushed up against the rotor blades by the air coming from below. Therefore, the tip vortices interfere with the rotor blades, which results in very high and rapidly varying induced velocities, also called the vortex ring state (VRS). As a consequence, the vibratory loads and associated aerodynamic noise are severely underpredicted [31]. Because of the inability of momentum theory of capturing other than laminar flow it is only valid in high rates of descend, where the stream around the rotor is along streamlines and outside the vicinity of the ground or obstacles, see sections 3.4 and 5.2.1.

In contrast to Momentum theory, which considers the rotor as a whole, Blade element theory (BET) is based on the blade geometry and has first been used by Drzewiecki, who assumed each blade section to behave independently. He discovered a significant error between his model and experimental data because he only used the average velocity upstream of the rotor disk and neglected the induced velocity caused by the rotation of the blades [23, 27]. Improvements to BET were made when Prandtl's Lifting line theory was included [23]. Drzewiecki never based his model on theory, however, when it was shown that the velocity potential for the potential flow relative to a rotating body at any cross section is equivalent to the two-dimensional nonrotating velocity potential his model was funded by theory [35] and experimentally proven by [36].

Blade element theory is based on modeling blade sections as a two-dimensional airfoil on which the induced and generated forces can be calculated. Integrating the forces over the entire blade and multiplying with the number of blades results in the rotor performance. Opposed to Momentum theory, which is only used to calculate the perpendicular velocity on the rotor disk, Blade element theory incorporates the drag and side force acting on the rotor. Based on the fact that BET is based on the geometry of the blades and MT on the rotor disk assumption, BET is more accurate in case of rotors with a small number of blades. However, BET is not capable of determining the rotor induced flow by itself and is therefore dependent on other theories, such as MT or vortex theory.

4.1.2 Dynamic inflow models

Whereas static inflow models neglect the dynamic interaction of the rotor to changes in blade pitch or flapping motion, dynamic inflow models try to incorporate these effects. The fundamental modeling principles of the dynamic inflow models rely on momentum theory. An extension into the dynamic field was first made by [37], who derived a differential equation that relates the perturbations in the inflow to the changes in rotor thrust [24] by including an apparent mass term in the thrust equation and linearisation around a steady-state condition.

The method was further developed by [38, 39] to make it valid for hover and forward flight by defining three different inflow states, uniform, longitudinal, and lateral. The airloads of a rotor, thrust (C_T), roll moment (C_{M_x}), pitch moment (C_{M_y}), are related to the induced flow distributions using the potential functions of Mangler and Squire [40]. The induced flow is assumed to be a linear distribution over the rotor disk and can be written as

$$\lambda = \lambda_0 + \frac{r}{R} \left(\sum_{k=1}^n \lambda_{k_s} \sin(k\psi) + \sum_{k=1}^n \lambda_{k_c} \cos(\psi) \right), \quad (4.4)$$

where $\lambda_0, \lambda_{k_s}, \lambda_{k_c}$ are the uniform, side-to-side, and fore-to-aft variation in induced flow. In [38, 39] an inflow distribution with $n = 1$ is developed, which relate the aerodynamic loads to the inflow in the following fashion

$$M \begin{pmatrix} \dot{\lambda}_0 \\ \dot{\lambda}_s \\ \dot{\lambda}_c \end{pmatrix} + VL^{-1} \begin{pmatrix} \lambda_0 \\ \lambda_s \\ \lambda_c \end{pmatrix} = \begin{pmatrix} C_T \\ C_{M_x} \\ C_{M_y} \end{pmatrix}, \quad (4.5)$$

where M is the apparent mass matrix, L the inflow gain matrix, and V the mass flow parameter matrix. Over the years several definitions for M , L and V have been defined depending on the flight conditions incorporated [24, 40–42]. The model is experimentally verified in [30]. A generalized theory with an arbitrary number of azimuthal and radial states is developed by [43, 44] based on the acceleration potential. The downside of this model is the fact that it only can calculate the vertical component of the induced velocity [45], while the in-plane components are of importance as well.

A second set of wake states is needed to calculate the flow off and on the disk. In [46] a generalized velocity potential is developed and expanded in terms of Legendre functions. These functions are converted to ordinary differential equations by using the Galerkin approach. A closed-form set of equations for all three velocity components everywhere in the upper hemisphere, including the rotor disk [45, 46] is obtained. However, the convergence of the model given in [46] was slow due to ill-conditioned matrices [45]. These issues were solved by [47] and their model is included into a dynamic inflow model. An extension is made by [45, 48] who developed a method to calculate the inflow below the plane of the rotor using the finite state method of [46].

The dynamic inflow models are fundamentally based on momentum theory, which implicates that the same restrictions apply, i.e. the models are not valid in the vortex ring state, in the vicinity of the ground and obstacles [24], and are only valid in hover and steady axial and forward flight. Furthermore, [38, 44] treated the rotor wake as quasi-steady in which wake bending due to pitch or roll is instantaneously. In practice the wake curvature, wake skew, and wake spacing develops in time.

Several researchers have tried to correct this by extending the model with a wake behavior model, such as [42] and [41]. Based on vortex tube analysis a four state reduced order wake model is introduced that captures the dynamic wake effects in transitional, maneuvering, and forward flight [24].

$$\tau_D \begin{pmatrix} \dot{X} \\ \dot{S} \\ \dot{\kappa}_c \\ \dot{\kappa}_s \end{pmatrix} + \begin{pmatrix} X \\ S \\ \kappa_c \\ \kappa_s \end{pmatrix} = \begin{pmatrix} X \\ S \\ \kappa_c \\ \kappa_s \end{pmatrix}_{qs}, \quad (4.6)$$

where X, S, κ_c, κ_s are the wake skew, wake spacing, longitudinal and lateral wake curvatures, respectively. The time constants associated with these dynamic wake distortion effect are include in the time constant matrix, τ_D . Generally the wake skew, wake spacing, longitudinal and lateral

wake curvatures, are fully coupled, however, are neglected in [41]. The time constant matrix can be defined as:

$$\begin{bmatrix} \frac{32}{15\pi\bar{V}} & & 0 & \\ & \frac{32}{15\pi V_m} & & \\ & & \frac{32}{15\pi\bar{V}} & \\ & 0 & & \frac{32}{15\pi\bar{V}} \end{bmatrix}, \quad (4.7)$$

with V_m and \bar{V} given by

$$\begin{aligned} V_m &= \sqrt{\mu^2 + (\lambda_0 + V_c)^2} \\ \bar{V} &= \frac{\mu^2 + (\lambda_0 + V_c)(2\lambda_0 + V_c)}{V_m}. \end{aligned} \quad (4.8)$$

The quasi steady wake parameters are given by

$$\begin{aligned} X_{qs} &= \tan\left(\frac{\chi}{2}\right) \\ S_{qs} &= 2\pi V_m \\ \kappa_{cqs} &= \frac{\bar{q} - \dot{\beta}_{1c}}{\lambda_0 + V_c} \\ \kappa_{sqs} &= \frac{\bar{p} - \dot{\beta}_{1s}}{\lambda_0 + V_c}, \end{aligned} \quad (4.9)$$

with the non dimensional roll and pitch rates denoted by \bar{p} and \bar{q} , and χ denotes the wake skew angle as defined in (4.2).

Nevertheless, still the vortex ring state and ground/obstacle effect are not accounted for. Semi-empirical modifications have been made to account for those flight conditions. A disadvantage of these models is that the modifications are add-ons and try to correct misbehavior of the original models. Furthermore, the wake models all contain tuning parameters to match the model with experimental results, however, this parameter can vary for different flight conditions [24, 41].

4.1.3 Vortex methods

Vortex methods model the rotor wake with help of vortex filaments. A vortex filament is a line along which an infinite vorticity in fluid motion is concentrated and the surrounding fluid is free of vorticity. These filaments are released from the blade and move downward into the wake. The induced velocities on the rotor can be calculated from the influence of each vortex segment in the wake using the Biot-Savart law. This law evaluates the induced velocity $d\vec{v}$ at a point P in the wake, a distance \vec{r} from a vortex segment with strength Γ_v and length $d\vec{l}$ [24]

$$d\vec{v} = \frac{\Gamma_v}{4\pi} \frac{d\vec{l} \times \vec{r}}{r^3}. \quad (4.10)$$

A first attempt to include the effect of the wake on the rotor and its influence on the performance is presented in [49], in which the wake is estimated with a helical surface for each blade, which moves downward with the average momentum theory velocity. However, effects of wake contraction and non-uniform downwash are not included. Later models try to remove those singularities, an overview is given in [50]. Most of these models use Prescribed or rigid wake models. Prescribed and rigid wake models are the simplest forms of vortex methods and use undistorted helical vortex filaments to describe the geometry of the wake. Feasible flight conditions in which these wake models can be used are steady state conditions, where changes in velocity or attitude can be neglected. In rigid wake models the rigid helical patterns keep a

fixed wake pitch without accounting for the effects of wake contraction, which is shown by momentum theory see section 5.2, viscosity and non-uniform downwash. In contrast to rigid wake models, prescribed wake models account for some degree of wake distortion. However, the wake is still assumed rigid and wake geometry parameters are extracted from experiments [25].

Contrary to prescribed and rigid wake models, free wake models allow the wake to deform freely under its own influence and influences due to translational and rotational velocities of the rotor. However, free wake models easily become computationally expensive. The velocity of a point on a vortex filament is influenced by all other vorticity carrying elements, resulting in a quadratic increase in computation time with the number of vortex elements [24]. Because of the inherent instability of the wake in hover and low-speed maneuvers numerical instabilities are likely to occur [24, 27, 51]. Different classifications of free wake models can be made. A classification presented in literature is based on the solution strategy and divides the free wake methods into two categories: relaxation and time marching approaches.

Relaxation methods use boundary conditions to relax the steady free wake solutions by enforcing periodicity [27]. Filaments released at the same point from subsequent blades deform equivalently and have a time offset of $2\pi/(\Omega N)$. Lagrangian markers track the position of the filaments in the discretized wake, which is discretized with respect to the blade azimuth ψ and the wake age ζ . To enforce periodicity, the new position of a vortex marker is the weighted average of the previous and the current solution [24]. This tracking is an iterative procedure which is repeated until the position of the markers have converged. As a consequence of the periodicity, relaxation based free wake models can only be used in steady-state flight conditions. A first attempt in modeling the wake of a rotor in hover is implemented in [52], in which the free wake is modeled using a relaxation method with a boundary at two rotor revolutions, after which the far wake is modeled using vortex rings. In [53] a predictor-corrector algorithm with a central differencing scheme is used for the space discretisation and extended into a two-step, pseudoimplicit predictor-corrector relaxation algorithm with five-point central differencing in space. A major drawback of this method is the necessity of computing the velocity field twice, however, it is more robust and less susceptible to numerical instabilities than one-step algorithms. Later on an adaptive grid sequencing and a velocity field interpolation scheme were developed to speed up the computation [24, 54]. The algorithm for computing the induced velocities contains a nonlinear implicit dissipation, which can make the numerical estimation unstable. By enforcing periodicity the numerical problems due to instabilities are avoided.

Time marching methods, in contrast to relaxation methods, can capture transient dynamics. As with relaxation based methods Lagrangian markers are used to track the position of the filaments in the discretize wake, however, the new position of the markers are found by time integration of the velocities [24]. The wake is allowed to deform under its own influence and external influences, such as turbulence, and no assumptions are made regarding periodicity. In [55, 56] the work of [53] is extended to be applicable to transitional manoevers as well. The predictor-corrector in [55, 56] contains a second-order backward difference algorithm (PC2B), with an additional dissipative term to cancel the nonlinear dissipation term of [53] and enforce wake stability. In [51] the algorithm of [55, 56] is enhanced by removing the predictor step and controlling the additional dissipative term to match the dissipative term of [53].

In [57] a Fast Free Wake (FFW) model is developed, which allows real-time simulations on a common desktop PC with margin for other simulations. The model is based on free wake models and use vortex rings to describe the wake. These rings are released with a certain frequency from the rotor disk. The vortex rings are free to move and to interact with each other on all other wake distortions. Each time step the position and orientation of the rings is updated until the ring is removed from the wake. The wake is modeled using a limited number of vortex rings to avoid computational expense. Because of the basis in free wake modeling the model is

applicable to all flight conditions, including in the vicinity of the ground and obstacles. This method can not be compared to more sophisticated methods because those are able to capture the wake dynamics in more detail, however, validation with respect to experiments shows the accuracy of the wake to be sufficient to account for wake interference effects independent of the flight conditions.

4.1.4 CFD methods

Computational Fluid Dynamics (CFD) is the numerical branch of fluid dynamics and has many applications areas. Generally CFD refers to grid-based solutions of the Navier-Stokes equations. Several simplifying assumptions can be made to the Navier-Stokes equations, such as Euler equations for inviscid flow or the full potential equation for potential flow. Following the work of [27] a subdivision can be made, shown in Figure 4.1, ranging from the full Navier-Stokes equations to the most simplified Laplace equations. The Laplace equation use the Biot-Savart law to solve the wake equations and show similarities with the vortex methods. A drawback of the CFD method is the computational expense needed for solving the wake equations, furthermore, most CFD solvers have excessive numerical dissipation of vorticity limiting the tracking of tip vortices to a couple of rotor revolutions. A possible solution is the use of a hybrid wake in which grid-based Navier-Stokes equations are used in the vicinity of the blades, i.e. near wake, and further down the wake simpler methods, such as Lagrangian methods, are used [24]. Combining this hybrid approach with the amount of possible wake equations and the various methods to discretize the wake, a large amount of different CFD based methods can be found in literature. Because of their complexity and computational expense the CFD methods are not realizable on quadrotors. Therefore they are outside the scope of this project and not further discussed.

4.2 Blade flapping models

In order to capture all the different blade dynamics during different flight regimes, several models on blade flapping have been developed using both first and second order approximations. Considering the flight regime of the quadrotor and the limited capacity of the AR drone's processor the benefits of including second order models are probably small and do not compensate for the added complexity.

Most blade flapping models are developed in helicopter theories [12–14, 18, 58]. All models are based on hinged rotors, assume rigid blades, and use moment balancing at the hinge to define the blade flapping angles. Furthermore, steady state is assumed in which the blade flapping angle can be approximated with a Fourier Series and the azimuth angle with, $\psi = \Omega t$. All authors claim that a hingeless or cantilevered rotor can be modeled as a hinged rotor with rigid blades and an effect hinge offset to account for the blade flexibility. In [14] the inertial force of the blades is neglected, because the centrifugal force is assumed to be in the plane of rotation and thereby eliminating the inertia force, and a weight force is included. All other models include the inertia force and neglect the weight force. Both [14] and [18] include the effect of pitching and rolling of the air-frame in the blade flapping characteristics.

In [12] it is discussed that the behavior of a two bladed rotor might be significantly different from rotors with three or more blades. It is claimed that a two bladed rotor behaves comparable to a teetering rotor, and the longitudinal and lateral flapping angles do not exist. This might be true for a rotor in transient flight, however, for steady state the behavior of a two blade rotor is the same as a three or more bladed rotor [59].

4.3 Concluding remarks

The more recent studies, such as, [9], [10], and [11], are based on the work of [60], in which the classical helicopter blade flapping model, based on [14], is adjusted to make it more suitable for small scale rotary wing platforms. Furthermore, as shown in section 3.6 the blade flapping dynamics are within one rotor revolution and have a much higher frequency than the rigid body behavior of the quadrotor, therefore, the blade flapping dynamics can be assumed instantaneously and steady state, which supports their choice for a steady state model. Based on their results and on the fact that the flapping behavior can be seen as steady state it is chosen to base the blade flapping model used in this thesis on [14].

The wake and inflow behavior is best captured with the vortex methods, however, these methods are mostly grid based and can become computational expensive. Based on experience with the CPU of the AR Drone and considering its limitations, implementing blade flapping together with Blade element theory and momentum theory might be maximum achievable. Blade element theory is incorporated because of the simplicity to include the rotor drag and side force and because it is a better representation of the two blade AR Drone rotors than the rotor disk assumption of Momentum theory.

Chapter 5

Theoretical model

In the previous chapters a basic knowledge level about inflow, wake and blade flapping behavior has been established. Several rotor parameters have been introduced and the inflow and wake states have been explained. In the previous chapter this knowledge is build upon in the search for suitable inflow, wake and blade flapping models. Based on the research and the limitations of the CPU of the AR DRone 2.0, it has been chosen to use Blade element theory combined with Momentum theory and the blade flapping model of [14] to model the inflow and blade flapping behavior. In this chapter the theory behind Blade element theory, Momentum theory, and blade flapping, is explained to create a deeper understanding of the fundamentals behind theses theories. Furthermore, an extended model is proposed to incorporate these aerodynamics in the rigid body dynamics of [5], see (2.2) and Section 5.4. The performance of this extended model is tested in simulations.

5.1 Blade Forces

The forces and moments acting on the blade can be modeled using Blade element theory (BET), which is based on lifting line theory and calculates the forces on the blade due to its motion through the air. Each blade section is assumed to act as a two dimensional airfoil which produces aerodynamic forces [12]. The influence of the wake on the rotor performance is accounted for by using an induced angle of attack. Blade element theory thus requires an estimate of the wake induced velocity at the rotor disk, which can be determined using, for example, momentum theory or vortex theory, see Chapter 5.2.

5.1.1 Hover and axial flight

The pitch angle of the blade section, θ is measured from the plane of rotation to the zero lift line, see Figure 5.1. As mentioned in Section 3.1 the pitch angle of a rotor with fixed pitch blades can be described by

$$\theta = \theta_0 + \frac{r}{R}\theta_{tw}. \quad (5.1)$$

The velocity relative to the blade consists of two components, the vertical or perpendicular velocity V_P and the tangential velocity V_T , and are defined by [12]

$$V_T = \Omega r \quad (5.2)$$

$$V_P = V_c + v_i. \quad (5.3)$$

The tangential velocity is due to the rotor speed and the perpendicular velocity is due to the climb velocity, V_c and the induced velocity, v_i . The resultant velocity acting on the blade, V , consists of V_P and V_T , and has an inflow angle, ϕ .

$$V = \sqrt{V_P^2 + V_T^2} \quad (5.4)$$

$$\phi = \arctan\left(\frac{V_P}{V_T}\right). \quad (5.5)$$

The local angle of attack, α_{bs} , consists of two angles, the pitch angle and the inflow angle and is defined as

$$\alpha_{bs} = \theta - \phi. \quad (5.6)$$

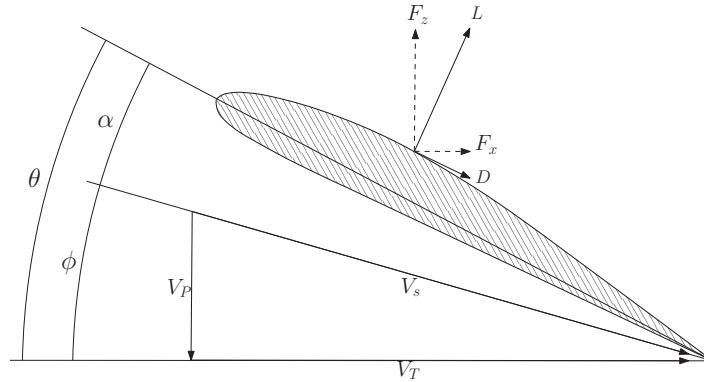


Figure 5.1: The aerodynamics of a blade section. The angle of attack, α_{bs} is the angle between the velocity V and the zero lift line. The blade section has a pitch angle, θ , which is measured from the plane of rotation to the zero lift line. The inflow angle is given by $\phi = \arctan(V_P/V_T)$

The lift and drag force a blade section generates is defined by [12, 13]

$$L = \frac{1}{2}\rho V^2 c C_l \quad (5.7a)$$

$$D = \frac{1}{2}\rho V^2 c C_d, \quad (5.7b)$$

where C_l and C_d are the lift and drag coefficient, and generally depend on the angle of attack and the mach number. The normal and in-plane forces can be derived as [12, 13]

$$F_z = L \cos(\phi) - D \sin(\phi) \quad (5.8a)$$

$$F_x = L \sin(\phi) + D \cos(\phi). \quad (5.8b)$$

The first term in F_x is the induced drag and the second term the profile drag. Substituting the definitions of the lift and drag force, given in (5.7a) and (5.7b), and dividing by the lift chord, c , and the two dimensional lift slope curve, a_0 , the force equations become

$$\frac{F_z}{a_0 c} = \rho V^2 \left(\frac{c_l}{2a_0} \cos(\phi) - \frac{c_d}{2a_0} \sin(\phi) \right) \quad (5.9a)$$

$$\frac{F_x}{a_0 c} = \rho V^2 \left(\frac{c_l}{2a_0} \sin(\phi) + \frac{c_d}{2a_0} \cos(\phi) \right). \quad (5.9b)$$

Assuming small angles [12], i.e. ϕ , θ are small, it follows that V_P/V_T and α are small, therefore

$$V^2 = V_T^2 \quad (5.10a)$$

$$\phi = \frac{V_P}{V_T} \quad (5.10b)$$

$$\alpha_{bs} = \theta - \frac{V_P}{V_T}. \quad (5.10c)$$

If the lift slope curve is assumed constant then the lift coefficient can be defined as, $c_l \cong a\alpha$ [12], neglecting the drag force only the normal force remains and is defined as

$$\frac{F_z}{a_0c} = \frac{1}{2}\rho V_T^2 \alpha = \frac{1}{2}V_T^2 \left(\theta - \frac{V_P}{V_T}\right). \quad (5.11)$$

The rotor forces are obtained by integrating the aerodynamic blade section forces along the span and multiplying with the number of blades. The thrust, T , is due to the normal force F_z and can be derived using

$$T = N \int_0^R F_z dr. \quad (5.12)$$

Rewriting into its coefficient form by dividing through by $\rho A(\Omega R)^2$ and using dimensionless quantities for ρ , Ω , and R , the thrust coefficient becomes [12]

$$\frac{C_T}{\sigma a_0} = \int_0^1 \frac{F_z}{a_0c} dr \quad (5.13a)$$

$$C_T = \frac{\sigma a_0}{2} \left[\frac{1}{3}\theta_0 + \frac{1}{4}\theta_{tw} - \frac{1}{2}\lambda \right]. \quad (5.13b)$$

In [4] experiments are performed to measure the thrust of each separate AR DRone rotor under hover conditions. The theoretical hover values therefore must comply with the experimental values. Because of the linear approximation of the blade twist, see Section 3.1, and some parameter uncertainties, the theoretically predicted thrust is slightly lower than the experimentally determined thrust, see Figure 5.2. An empirical correction factor, κ_T , is introduced to match the theoretical with the experimental thrust

$$\kappa_T = \frac{T_{exp}}{T_{th}}. \quad (5.14)$$

The adjusted thrust coefficient can be written as

$$C_T = \kappa_T \frac{\sigma a_0}{2} \left[\frac{1}{3}\theta_0 + \frac{1}{4}\theta_{tw} - \frac{1}{2}\lambda \right]. \quad (5.15)$$

5.1.2 Forward flight

In forward flight the rotor blades not only experience their own rotational speed, a component of the quadrotor's velocity acts on the blade as well, see section 3.6. On the advancing blade the quadrotor's velocity is added to the rotational velocity, where on the retreating blade the quadrotor's velocity is subtracted from the rotational velocity. In contrast to the axial case the blade velocities now depend on the blade position defined with the azimuth angle, ψ_b .

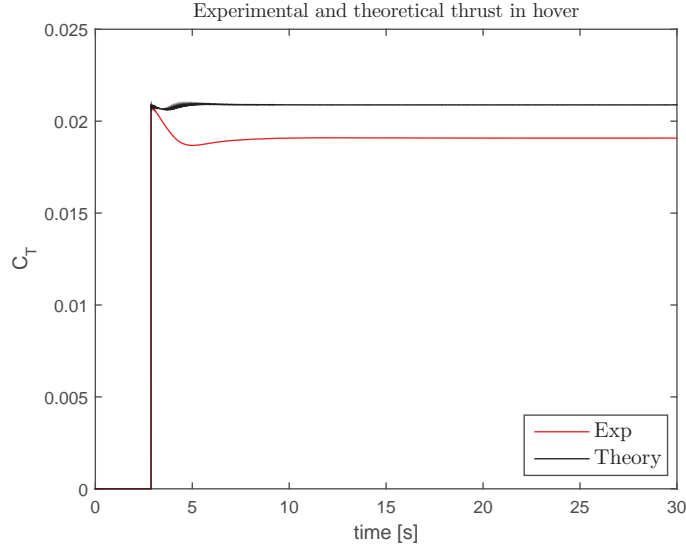


Figure 5.2: Experimental [4] and theoretical determined thrust in hover flight for one rotor.

The velocity relative to the blade consists of three components, the perpendicular velocity V_P , the tangential velocity V_T , and the radial velocity, V_r , which can be defined as [12]

$$V_T = r + \mu \sin(\psi) \quad (5.16a)$$

$$V_R = \mu \cos(\psi) \quad (5.16b)$$

$$V_P = \lambda + r\dot{\beta} + \beta\mu \cos(\psi), \quad (5.16c)$$

where it has been assumed that the flap angle β is small. The tangential and radial velocity both are due to the rotor speed and the advance ratio of the quadrotor. Three components contribute to the perpendicular velocity. The induced velocity and a component of the free stream velocity normal to the rotor disk, defined as λ , see sections 3.4 and 5.2, the blade flapping velocity represented by $r\dot{\beta}$, and a component of the radial velocity when it is flapped up by an angle β .

The contribution of the flapping motion to the perpendicular velocity can be derived as $r'\dot{\beta}$, with

$$\dot{\beta} = \frac{d\psi}{dt}(\beta_{1s} \sin(\psi) - \beta_{1c} \cos(\psi)) \quad (5.17)$$

and

$$\frac{d\psi}{dt} = \frac{d}{dt}(\Omega t) = \Omega. \quad (5.18)$$

Note that this relation only holds when the rotor speed is constant, which is the case for helicopters, however, for quadrotors this might be difficult to achieve.

The normal and in-plane forces can be derived as [12, 13]

$$F_z = L \cos(\phi) - D \sin(\phi) \quad (5.19a)$$

$$F_x = L \sin(\phi) + D \cos(\phi) \quad (5.19b)$$

$$F_r = -\beta F_z + D_{\text{radial}}. \quad (5.19c)$$

The first term in F_r is due to blade flapping and the second term is due to the radial flow along the blade. Substituting the definitions of the lift and drag force, given in (5.7a) and (5.7b), and

dividing by the lift chord, c , and the two dimensional lift slope curve, a , the force equations become

$$\frac{F_z}{a_0 c} = V^2 \left(\frac{c_l}{2a_0} \cos(\phi) - \frac{c_d}{2a_0} \sin(\phi) \right) \quad (5.20a)$$

$$\frac{F_x}{a_0 c} = V^2 \left(\frac{c_l}{2a_0} \sin(\phi) + \frac{c_d}{2a_0} \cos(\phi) \right) \quad (5.20b)$$

$$\frac{F_r}{a_0 c} = -\beta \frac{F_z}{a_0 c}, \quad (5.20c)$$

where D_{radiaal} has been neglected [12, 13].

Assuming again, as in the axial case, small angles, a constant lift curve slope, and neglecting stall, the aerodynamic force can be rewritten as

$$\frac{F_z}{a_0 c} = \frac{1}{2} V_T^2 \alpha = \frac{1}{2} (V_T^2 \theta - V_P V_T) \quad (5.21a)$$

$$\frac{F_x}{a_0 c} = V_T^2 \left(\frac{\alpha}{2} \phi + \frac{c_d}{2a_0} \right) = \frac{1}{2} (V_P V_T \theta - V_P^2) + \frac{c_d}{2a_0} V_T^2 \quad (5.21b)$$

$$\frac{F_r}{a_0 c} = -\beta \frac{F_z}{a_0 c}. \quad (5.21c)$$

The rotor forces are obtained by integrating the aerodynamic blade section forces along the span and multiplying with the number of blades. The thrust, T , is due to the normal force F_z and the drag and side force, respectively H and Y , are due to the in-plane forces F_x and F_r .

$$T = N \int_0^R F_z dr \quad (5.22a)$$

$$H = N \int_0^R (F_x \sin(\psi) + F_r \cos(\psi)) dr \quad (5.22b)$$

$$Y = N \int_0^R (-F_x \cos(\psi) + F_r \sin(\psi)) dr. \quad (5.22c)$$

The velocities on the blades are dependent on the position with respect to the free stream velocity. To obtain a steady rotor force the forces are averaged over the azimuth by the operator $(1/2\pi) \int_0^{2\pi} (...) d\psi$ [12]. Rewriting each equation into the coefficient form results in

$$\frac{C_T}{\sigma a_0} = \frac{1}{2\pi} \int_0^1 \int_0^{2\pi} \frac{F_z}{a_0 c} d\psi dr \quad (5.23a)$$

$$\frac{C_H}{\sigma a_0} = \frac{1}{2\pi} \int_0^1 \int_0^{2\pi} \left(\frac{F_x}{a_0 c} \sin(\psi) + \frac{F_r}{a_0 c} \cos(\psi) \right) d\psi dr \quad (5.23b)$$

$$\frac{C_Y}{\sigma a_0} = \frac{1}{2\pi} \int_0^1 \int_0^{2\pi} \left(-\frac{F_x}{a_0 c} \cos(\psi) + \frac{F_r}{a_0 c} \sin(\psi) \right) d\psi dr. \quad (5.23c)$$

For the thrust coefficient the following derivation is required

$$\begin{aligned}
\frac{1}{2\pi} \int_0^{2\pi} V_P V_T d\psi &= \frac{1}{2\pi} \int_0^{2\pi} (\lambda + r\dot{\beta} + \mu\beta \cos(\psi)) + (r + \mu \sin(\psi)) d\psi \\
&= \frac{1}{2\pi} \int_0^{2\pi} (\lambda r + \mu\lambda \sin(\psi) + r^2\dot{\beta} + r\mu\dot{\beta} \sin(\psi) + r\mu\beta \cos(\psi) + \frac{1}{2}\beta\mu^2 \sin(2\psi)) \psi d\psi \\
&= \frac{1}{2\pi} \int_0^{2\pi} (\lambda r + \mu\lambda \sin(\psi) + \frac{d}{dt}(r^2\beta + r\mu\beta \sin(\psi)) + \frac{1}{2}\beta\mu^2 \sin(2\psi)) \psi d\psi \\
&= \frac{1}{2\pi} \int_0^{2\pi} (\lambda r + \frac{1}{2}\beta\mu^2 \sin(2\psi)) \psi d\psi \\
&= \lambda r,
\end{aligned}$$

where it has been used that

$$\int_0^{2\pi} \left(\frac{d}{dt} (r^2\beta + r\mu\beta \sin(\psi)) \right) d\psi = 0, \quad (5.24)$$

since the term inside the bracket is periodic because steady state conditions are assumed [12].

Performing the same derivations for the drag and side force, performing the integral over the span, and including the correction factor for the thrust the force coefficients become [12]

$$C_{T_{TPP}} = \kappa_T \frac{\sigma a_0}{2} \left[\theta_0 \left(\frac{1}{3} + \frac{1}{2}\mu^2 \right) + \theta_{tw} \left(\frac{1}{4} + \frac{1}{4}\mu^2 \right) - \frac{1}{2}\lambda \right] \quad (5.25a)$$

$$C_{H_{TPP}} = \frac{1}{4}\mu c_{d_0} + \frac{\sigma a_0}{2} \left[\frac{1}{2}\mu\lambda \left(\theta_0 + \frac{1}{2}\theta_{tw} \right) + \frac{1}{4}\mu\beta_0^2 \right] \quad (5.25b)$$

$$C_{Y_{TPP}} = -\frac{\sigma a_0}{2} \left[\frac{3}{4}\mu\beta_0 \left(\theta_0 + \frac{2}{3}\theta_{tw} \right) - \frac{3}{2}\mu\beta_0\lambda \right], \quad (5.25c)$$

where c_{d_0} is the zero-lift drag coefficient, which is usually small for rotor blades and can be neglected.

Forces acting on the quadrotor should be expressed in the body fixed frame, therefore the rotor forces in the TPP are expressed within the HP, which is aligned with the wind axis frame, \mathcal{C} , and thereafter transformed to the body fixed frame using the Rotation matrix R_{cb} defined in (3.5). The transformation from the TPP to the HP for the in-plane forces can be described by the rotation matrix R_{HT} ,

$$\begin{bmatrix} H_{HP} \\ Y_{HP} \end{bmatrix} = R_{TH} \begin{bmatrix} H_{TPP} \\ Y_{TPP} \end{bmatrix}, \quad (5.26)$$

with

$$R_{TH} = \begin{bmatrix} \cos(\beta_{1_c}) & 0 \\ 0 & \sin(\beta_{1_s}) \end{bmatrix}, \quad (5.27)$$

where β_{1_c} and β_{1_s} are the longitudinal and lateral blade flapping angles following from the Fourier series. In the section about blade flapping the rotation matrix for the thrust vector is discussed. Note that the rotor forces in forward flight reduce to the axial forces when the forward flight equals zero, i.e. $\mu = 0$, which shows that the definition for forward flight has the proper lower bound.

5.1.3 Combined flight

The two separated cases of axial and forward flight need to be combined in order to perform a three dimensional flight. In deriving the forces for combined flight the velocities on the blade need to be redefined. The tangential and radial velocity are the same as in the forward flight case, however, the perpendicular velocity needs to be adjusted to account for the climb or descent velocity, V_c . The climb velocity is integrated in the inflow ratio, see Section 5.2.3, and is defined as

$$\lambda = \mu_c + \mu \tan(\alpha_d) + \lambda_i, \quad (5.28)$$

where

$$\mu_c = \frac{V_c}{\Omega R}. \quad (5.29)$$

With the climb velocity accounted for in the inflow ratio, the expression and the derivation for the rotor forces are the same as in the forward flight case. Note that when $\mu_c = 0$ the expression for the perpendicular velocity reduces to the forward flight case and when $\mu = 0$ the expression becomes equal to the axial flight case, which shows the proper bounds.

5.1.4 Comments on Blade element theory

Blade element theory is based on the lifting line theory and is valid for incompressible, frictionless, steady flows, which are the same assumptions used in Momentum theory. The steady flow assumption is made for modeling purposes, however, is in reality not applicable. Several other assumptions are made during the derivations based on the rotor blade dynamics.

Assumption 5.1.1. *In the derivation of BET the following assumptions are used:*

- (i) *The flow is steady*
- (ii) *The flow is incompressible*
- (iii) *The flow is frictionless*
- (iv) *The disk loading is low*
- (v) *The angles are small*
- (vi) *The lift slope curve is constant*

The small angle assumption is made to simplify the calculations and to be able to perform the derivations. Figure 5.3 shows the simulation result for both angles for a quadrotor perfectly following the reference trajectory, described by

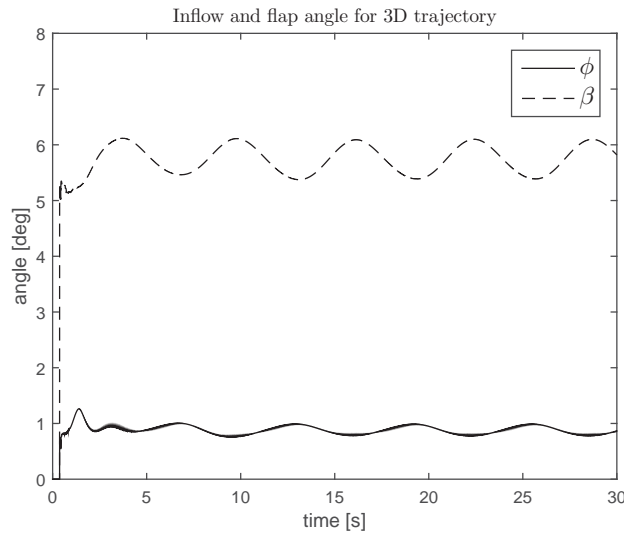
$$\rho_r = [\cos(t) \quad \sin(t) \quad 1.5 + \sin(t)]^T, \quad (5.30)$$

which is the same as the 3D trajectory used in the experiments of Section 2.3 and the simulations of Section 5.5. The parameters described in Table 5.1 are used in the simulation and the angles are measured at the tip, i.e $r = 1$.

From the figure it can be seen that the small angle assumption is valid. It might seem that the blade flap angle does not satisfies this assumption, however, the blade angle is always operated on with a sine or cosine term, which makes the values close to zero and one and therefore the assumption is valid. The figure shows the results for the maximum blade flap angle, which is at $\psi_\beta = \pi$, and the maximum inflow angle, which is at $\psi_{phi} = -1/2\pi$.

Table 5.1: Simulation parameters for the simulation performed for Figure 5.3.

Parameter	Value
a_0	5.7
A	0.031
c	0.018
e_f	0.2
I_b	5.29×10^{-6}
m	0.036
r	1
γ	2.409
θ_0	0.646
θ_{tw}	-0.436
σ	0.134

**Figure 5.3:** The flap angle β and inflow angle ϕ at $\psi_\beta = \pi$ and $\psi_{phi} = -1/2\pi$

5.2 Inflow

An important aspect in rotor aerodynamics are the induced velocities at and near the rotor. A turning rotor produces thrust by accelerating mass of air [14, 29, 61]. The air sucked in is accelerated as it goes through the rotor and generates an induced airflow. The behavior of the induced airflow in the wake of the rotor influences the behavior of the rotor and the air above the rotor. The influence of induced velocities in the quadrotor's dynamics is dual, determines the amount of thrust a rotor can produce and generates drag and side forces acting on the rotor hub, see Section 5.1. Furthermore, it influences the blade flapping characteristics, see Section 5.3.

Momentum theory for rotary wing vehicles was developed by Glauert, in 1962, based on earlier work by Froude for aircraft propellers [29, 61]. The theory considers a rotor as an actuator disc, a circular surface with zero thickness which can support a pressure difference, with the accelerating air forming a stream tube, see Figure 5.4. Momentum theory uses the three energy conservation laws, conservation of mass, energy, and momentum, to relate induced velocity at the rotor disk to the thrust. In momentum theory the disk loading is assumed to be uniform and steady, however, in general the flow varies across the disk and vortices are likely to occur.

Furthermore, the actuator disk model represents a rotor with an infinite number of blades, therefore, the detailed flow is different from a real rotor with a small number of blades.

5.2.1 Hover and vertical flight

Combining a control volume with the conservation laws results in relations that can be analyzed for different cross sections. Figure 5.4 shows two streamtubes for hover and axial flight analysis. The left streamtube is used in the analysis for hover and climbing flight, while the right streamtube is used in descent flight analysis. For the analysis given below a NED inertial reference frame is used where the positive z -direction is indicated by the red arrows. Note that in climb the climb rate equals $-V_c$ and in descent equals V_c .

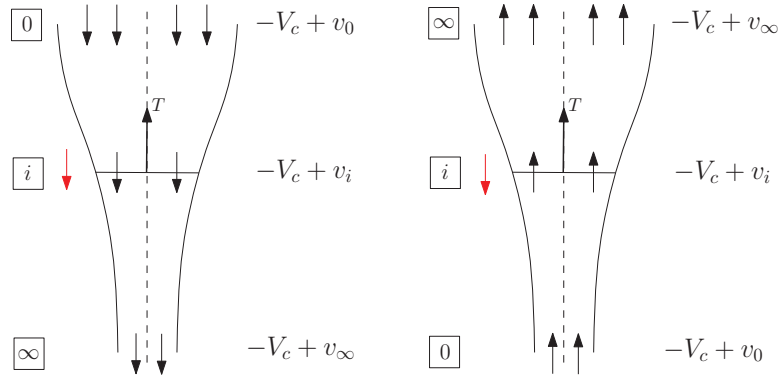


Figure 5.4: Vertical streamtube for hover and axial flight analysis. The left streamtube is for hover and climb analysis and the right streamtube is used for descent analysis. Both streamtubes have three sections, namely: upstream (0), at the rotor disk (i), and downstream (∞) with their corresponding variables.

The control volume definition of the conservation of mass is stated as [62]:

$$\frac{dM}{dt} = \frac{\partial}{\partial t} \int_{CV} \rho dV + \int_{CS} \rho \vec{V} \cdot d\vec{A} = 0, \quad (5.31)$$

where dM/dt is the mass flux, ρ is the density of air inside the control volume, \vec{V} is the velocity of air, $d\vec{A}$ is the area element the integral is acting on, V is the volume of the control volume, CV is the control volume and CS is the surface of the control volume, i.e. the control surface. Under certain conditions, stated below in Assumption 5.2.1, this can be reduced to:

$$\rho \int_{CS} \vec{V} \cdot d\vec{A} = 0, \quad (5.32)$$

which means that for a steady flow the mass flow rate into the control volume must equal the mass flow rate out of the control volume. Note that outflows are positive and inflows are negative. Using the definitions in Figure 5.4, (5.32) can be rewritten as

$$\rho A_0(-V_c + v_0) = \rho A_\infty(-V_c + v_\infty) = \rho A_i(-V_c + v_i), \quad (5.33)$$

where V_c is the climb velocity and v_0 , v_i , and v_∞ are the induced velocities at their respective stages. The definition of (5.33) corresponds to the definition given in helicopter theory [12, 13].

Momentum conservation states that the sum of all forces acting on a non-accelerating control volume equals the sum of the rate of change of momentum inside the control volume and the

net rate of flux of momentum out through the control surface [62]

$$\frac{dP}{dt} = \sum F = \frac{\partial}{\partial t} \int_{CV} \vec{V} \rho dV + \int_{CS} \vec{V} \rho \vec{V} \cdot d\vec{A}, \quad (5.34)$$

which can be reduced to

$$\sum F = \int_{CS} \vec{V} \rho \vec{V} \cdot d\vec{A}. \quad (5.35)$$

Since the force acting on the control volume is equal and opposite to the rotor thrust, and steady and uniform flow is assumed, (5.35) becomes

$$T = -(\rho A_\infty (-V_c + v_\infty)^2 - \rho A_0 (-V_c + v_0)^2). \quad (5.36)$$

Using mass conservation the reduced form can be rewritten into

$$\begin{aligned} T &= -\rho A_i (-V_c + v_i) (-V_c + v_\infty) + \rho A_i (-V_c + v_i) (-V_c + v_0) \\ &= -\rho A_i (-V_c + v_i) (v_\infty - v_0). \end{aligned} \quad (5.37)$$

The law of conservation of energy applicable to a control volume can be stated as [62]

$$\dot{Q} - \dot{W} = \frac{\partial}{\partial t} \int_{CV} e \rho dV + \int_{CS} e \rho \vec{V} \cdot d\vec{A}, \quad (5.38)$$

with

$$e = u + \frac{V^2}{2} + gz. \quad (5.39)$$

Applying the same assumptions as used in the case of mass and momentum conservation and assuming no heat is added to or subtracted from the system, (5.38) becomes

$$-\dot{W} = \int_{CS} e \rho \vec{V} \cdot d\vec{A}. \quad (5.40)$$

The work done on the surroundings by the control volume is equal to the work done by the rotor on the surroundings, which equals $\dot{W} = T\vec{V}$. Neglecting the height difference within the control volume, and assuming the air behaves as an ideal gas with no temperature difference inside the streamtube

$$-T(-V_c + v_i) = \frac{1}{2} \rho A_\infty (-V_c + v_\infty)^3 - \frac{1}{2} \rho A_0 (-V_c + v_0)^3, \quad (5.41)$$

which is the relationship as established in helicopter theory [12, 13]. Note that the thrust from itself is negative, which makes the left hand side positive as power needs to be delivered to maintain a hover or climbing flight. This reduced form can be rewritten, using mass conservation (5.33), into

$$\begin{aligned} -T(-V_c + v_i) &= \frac{1}{2} \rho A_i (-V_c + v_i) (-V_c + v_\infty)^2 - \frac{1}{2} \rho A_i (-V_c + v_i) (-V_c + v_0)^2 \\ T &= -\frac{1}{2} \rho A_i (-2V_c + v_0 + v_\infty) (v_\infty - v_0). \end{aligned} \quad (5.42)$$

Because only the variables at the rotor are known, an expression for the thrust in rotor variables is needed in order to calculate the amount of thrust the rotor can produce. A relationship between v_i and v_∞ can be derived using equations (5.37) and (5.42)

$$\begin{aligned} 2(-V_c + v_i)(v_\infty - v_0) &= (-2V_c + v_0 + v_\infty)(v_\infty - v_0) \\ v_\infty &= 2v_i - v_0. \end{aligned} \quad (5.43)$$

Assuming the velocity far upstream is approximately zero, $v_0 \approx 0$, and using (5.43), the rotor induced velocity can be expressed as

$$v_i = \frac{V_c}{2} + \sqrt{\left(\frac{V_c}{2}\right)^2 - \frac{T}{2\rho A}}, \quad (5.44)$$

which can also be found in helicopter literature [12–14]. Note that for hovering conditions this definition also holds and can be taken into account by setting the climb velocity equal to zero

$$v_i = v_h = \sqrt{-\frac{T}{2\rho A}}. \quad (5.45)$$

Normalizing with the tip speed, dividing by ΩR , results in

$$\lambda_i = \lambda_h = \sqrt{-\frac{T}{2\rho A(\Omega R)^2}} = \sqrt{-\frac{C_T}{2}}, \quad (5.46)$$

where the definition of the thrust coefficient is used, given in Section 3.2.

Implementing the relationship of the induced wake and induced rotor velocity (5.43) into the mass conservation law (5.33), and considering the hover case, i.e. $V_c = 0$, results in

$$\rho A_\infty 2v_i = \rho A_i v_i. \quad (5.47)$$

Under the assumption of ρ to be constant throughout the wake, this equation can only hold if

$$A_\infty = \frac{1}{2}A_i, \quad (5.48)$$

which is called wake contraction. As mentioned in Section 4.1.3 prescribed and rigid wakes models do not inherent wake contraction and thereby neglect an important part of the wake behavior.

In the derivation of the reduced order forms of the conservation laws, assumptions are made to be able to define an expression for the rotor inflow.

Assumption 5.2.1. *Momentum theory for hover or axial flight uses the following assumptions to derive a expression for the induced inflow*

- (i) *flow is steady*
- (ii) *flow is incompressible*
- (iii) *flow is along a streamline*
- (iv) *flow is frictionless*
- (v) *flow is uniform at cross section*
- (vi) *flow is derived with respect to an inertial control volume*

The climb model is not valid for the descent case as the free stream velocity is directed upward and therefore the far downstream wake is above the rotor disk, see Figure 5.4. Note that the order of the stages is reversed because the downstream wake is above the rotor disk. Because of this stage reversal the derivation for both climb and descent is the same. There exists, however, a region in which neither of the two models is valid.

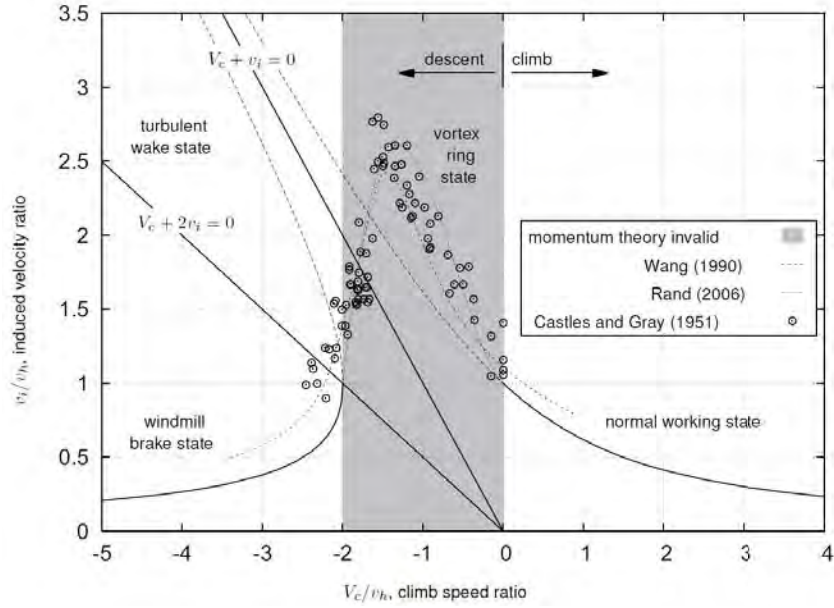


Figure 5.5: Rotor induced velocity as a function of climb speed ratio, showing the different branches in descent flight and experimental data from Castles and Gray obtained in the vortex ring state [24].

In climb the flow must be downward and therefore the velocity at stage zero and in the far wake must be positive, i.e. $-V_c + v_0 \geq 0$ and $-V_c + v_\infty = -V_c + 2v_i \geq 0$, which imply $-V_c \geq 0$ and $-V_c \geq -2v_i$, resulting in $-V_c \geq 0$, defining the climb model to be only valid in climb. In descent the flow is upwards and therefore the velocity in the far wake velocity and at stage zero must be negative, i.e. $-V_c + v_0 \leq 0$ and $-V_c + v_\infty = -V_c + 2v_i \leq 0$, implying that the descent velocity must be larger then $-V_c \leq -2v_i$. The boundaries for the validity of Momentum theory are found in literature and shown in Figure 5.5. The line $V_c + v_i$ is the boundary between the vortex ring state and the turbulent wake state. From the data of [63] in the vortex ring state a certain trend in the induced velocity can be discovered. It is worth investigating if such a trend can also be discovered for quadrotors.

5.2.2 Forward flight

Rotors of a quadrotor are required to produce both a lifting L and forward P force to counteract the weight and propel to quadrotor forward, see Figure 5.6. Therefore, the rotor disk must tilt forward with an angle of attack, α_d , with respect to the oncoming flow. Induced flow decreases as the aircraft's forward speed increases. A simplistic explanation, when the helicopter is in hover all the induced flow comes vertically down through the disc. If a wind blows, part of the down going induced flow would be blown away horizontally, resulting in less air flowing through the disc vertically.

Figure 5.6 shows the streamtube which is used in forward flight analysis. In deriving the conservation laws a NED inertial frame is used, with the vertical axis parallel to the thrust vector and its positive direction indicated by the red arrow in Figure 5.6. Note that in forward flight analysis only horizontal flight is taken into account.

Where in hover and axial flight the streamlines are perpendicular to the rotor disk, in forward flight this may not be the case. However, it is assumed that at the rotor disk the angle of attack, α_d , is the angle of the disk with respect to the free stream velocity, V . Since only the velocity

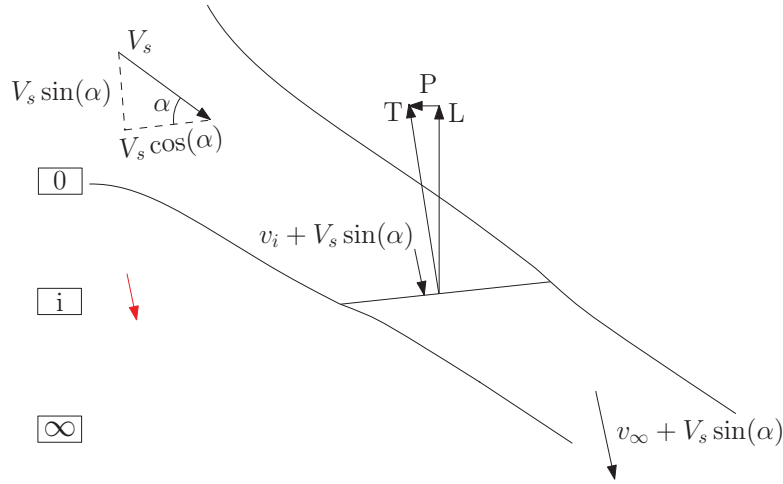


Figure 5.6: Streamtube for forward flight analysis. Three sections are shown, namely: up-stream (0), at the rotor (i), and down stream (∞) with their corresponding variables. The red arrow indicates the positive z -direction of a NED inertial frame. T is the thrust, L is the lift force and P is the propulsive force

perpendicular to the rotor disk contributes to the thrust, it is only necessary to evaluate the vertical direction.

In the analysis of induced velocity in forward flight again a uniform loaded actuator disk is used to model the behavior of the rotor. In forward flight the actuator disk may be viewed as a circular wing, of which it can be proven, using classical fixed-wing lifting-line theory, that for high speed forward flight the thrust is equal to [12, 13]

$$v_i = -\frac{T}{2\rho A_i V}. \quad (5.49)$$

An expression for the rotor thrust in hover and high speed forward flight is developed, however, a connection between those two regions is required to specify the thrust and inflow for all operating conditions.

Using the definitions for the control volume conservation laws as given in (5.31), (5.34), (5.38) and applying the same assumptions as for hover and axial flight, the control laws reduce to their reduced forms as given in (5.32), (5.35), (5.41). Applying the reduced forms, the law for conservation of mass in forward flight becomes

$$\rho A_0 V_{r_0} = \rho A_i V_{r_i} = \rho A_\infty V_{r_\infty}, \quad (5.50)$$

where V_r is the resultant velocity, a combination of the free stream velocity V and the induced velocity v_i , and can be defined at the rotor disk as [12]

$$V_{r_i}^2 = (V \cos(\alpha_d))^2 + (V \sin(\alpha_d) + v_i)^2 = V^2 + 2Vv_i \sin(\alpha_d) + v_i^2. \quad (5.51)$$

The momentum equation, is slightly different from the case of hover and climb because the rotor disk is tilted with an angle of attack with respect to the free stream velocity. Therefore the sine component of the free stream velocity, which is along the vertical axis of the NED frame, is taken into account. The momentum equation can be written into scalar component equations of which only the vertical direction is evaluated.

$$\sum F_3 = \int_{CS} V_3 \rho \vec{V} \cdot dA. \quad (5.52)$$

The reduced momentum equation combined with the mass equation results in

$$\begin{aligned} T &= -[\rho A_i V_{r_i}(v_\infty + V \sin(\alpha)) - \rho A_i V_{r_1}(v_0 + V \sin(\alpha))] \\ &= -\rho A_i V_{r_i}(v_\infty - v_0). \end{aligned} \quad (5.53)$$

The work done by the rotor on the surroundings equals $W_r = TV_3$. Therefore, the reduced energy law combined with mass conservation, becomes

$$-T(v_i + V \sin(\alpha)) = \frac{1}{2} \rho A_i V_{r_i}(v_\infty^2 + 2Vv_\infty \sin(\alpha) - 2Vv_0 \sin(\alpha) - v_0^2). \quad (5.54)$$

To establish a relation between v_∞ and v_i , (5.54) and (5.53) are combined.

$$\begin{aligned} 2(v_\infty - v_0)(v_i + V \sin(\alpha)) &= v_\infty^2 + 2Vv_\infty \sin(\alpha) - 2Vv_0 \sin(\alpha) - v_0^2 \\ 2v_\infty v_i &= v_\infty^2 \\ v_\infty &= 2v_i, \end{aligned} \quad (5.55)$$

where it is assumed that $v_0 \approx 0$ as in the climb case. Using this relation in (5.53) and making use of (5.45), the expression for the induced velocity becomes [12, 13]

$$v_i = \frac{v_h^2}{\sqrt{(V \cos(\alpha))^2 + (V \sin(\alpha) + v_i)^2}}. \quad (5.56)$$

Note that for hovering flight, $V = 0$, so that the equation reduces to

$$v_i = v_h = \sqrt{\frac{T}{-2\rho A_i}}, \quad (5.57)$$

which confirms that the forward flight case reduces to the hover flight and has the proper lower bound. In high speed forward flight $V \gg v_i$ and the equation reduces to

$$v_i = -\frac{T}{2\rho A_i V}. \quad (5.58)$$

This is exactly the lift on an elliptically loaded fixed-wing, see (5.49), which shows that the established relationship for the thrust has the proper upper bound.

If (5.56) is normalized with the tip speed and the normalized velocity components are used, defined in (3.6) and (3.7), the induced inflow ratio becomes

$$\lambda_i = \frac{C_T}{2\sqrt{\mu^2 + \lambda^2}}. \quad (5.59)$$

Substituting (5.59) into (3.7) results in a definition for the inflow ratio

$$\lambda = \mu \tan(\alpha_d) + \frac{C_T}{2\sqrt{\mu^2 + \lambda^2}}. \quad (5.60)$$

The result is a quartic equation in λ which can be solved analytically, however, the thrust coefficient C_T depends on λ as well. Therefore, λ is solved iteratively in combination with C_T using a Newton-Raphson iterative procedure. The iteration scheme can be defined as [12, 13]

$$\lambda_{n+1} = \lambda_n - \frac{f(\lambda)}{f'(\lambda)}, \quad (5.61)$$

with

$$f(\lambda) = \lambda - \mu \tan(\alpha_d) - \frac{C_T}{2\sqrt{\mu^2 + \lambda^2}} = 0. \quad (5.62)$$

This results in the iteration scheme [12, 13]

$$\lambda_{n+1} = \left(\frac{\mu \tan(\alpha_d) + \frac{C_{T_n}(\mu^2 + 2\lambda_n^2)}{2(\mu^2 + \lambda_n^2)^{3/2}}}{1 + \frac{C_{T_n} \lambda_n}{2(\mu^2 + \lambda_n^2)^{3/2}}} \right), \quad (5.63)$$

with

$$\lambda_0 = \mu \tan(\alpha_d) + \frac{C_T}{2\sqrt{\mu^2 + \frac{C_T}{2}}}, \quad (5.64)$$

and C_{T_0} equal to the thrust coefficient in hover. Note that this procedure is not valid when the rate of descent is sufficient to enter the vortex ring state. Generally λ converges, however, nonphysical solutions may be obtained [13]

5.2.3 Combined flight

Including the climb velocity into the resultant velocity V_r leads to the same expression for the mass conservation as in forward flight, given in (5.33). The resultant velocity V_r at the rotor disk is redefined as:

$$V_{r_i}^2 = (V \cos(\alpha))^2 + (V \sin(\alpha) + v_i - V_c)^2, \quad (5.65)$$

It can be shown, using the same procedure as in forward flight, that in the combined case the wake induced velocity is twice the rotor induced velocity, $v_\infty = 2v_i$, the same as in the axial and forward flight cases. Substituting this into (5.53) and using the new definition for V_r results in:

$$T = -2\rho A_i v_i \sqrt{(V \cos(\alpha))^2 + (V \sin(\alpha) + v_i - V_c)^2}, \quad (5.66)$$

which can be rewritten into:

$$v_i = \frac{v_h^2}{\sqrt{(V \cos(\alpha))^2 + (V \sin(\alpha) + v_i - V_c)^2}}. \quad (5.67)$$

Using the definition for the advance ratio (3.6), and defining the inflow ratio as:

$$\lambda = \mu_c + \mu \tan(\alpha_d) + \lambda_i, \quad (5.68)$$

where

$$\mu_c = \frac{V_c}{\Omega R}, \quad (5.69)$$

the induced inflow ratio becomes

$$\lambda_i = \frac{C_T}{2\sqrt{\mu^2 + \lambda^2}}, \quad (5.70)$$

which is again a quartic equation in λ and can be solved using the same procedure as in the forward flight case.

5.2.4 Comments on Momentum theory

Momentum theory is based on the actuator disk model. This model approximates the rotor by a thin disk. In case of the AR Drone, however, the rotor consists of two blades. The detailed behavior of the flow around the rotor is therefore probably different than estimated with momentum theory. In order to derive the reduced conservation laws several assumptions have been made. One of these assumptions is that the laws are derived with respect to an inertial reference frame. Meaning the mass, momentum and energy relations do not account for the acceleration of the frame. However, tracking a trajectory means constantly accelerating and decelerating. Furthermore, the quadrotor is constantly updating its orientation and thereby rotating with respect to an inertial frame. The conservation laws thus need to be extended to be applicable to a rotating frame as well.

The flow is assumed to be steady and uniform at a random cross-section of the control volume and the flow is along streamlines. In reality, however, the flow, especially in forward flight, is not uniform. Furthermore, the rotor produces tip vortices, which influence the flow behavior in the near and far wake. The near wake influences the blade's airloads and the rotor's inflow behavior, consequently, the tip vortices play an important role in the rotor aerodynamics and should not be neglected.

Figure 5.7 shows the thrust estimation for the height varying trajectory of (2.6) for BET/MT, MT and experimentally determined by Jeurgens. In Section 5.5 it is shown that the combination of BET and MT is capable of estimating the z -dynamics accurately enough. From the figure it can be seen that MT overestimates the required thrust and the experimentally determined thrust underestimates the required thrust. The combination of BET and MT is capable of accurately estimating the required thrust, as will be shown in Section 5.5.

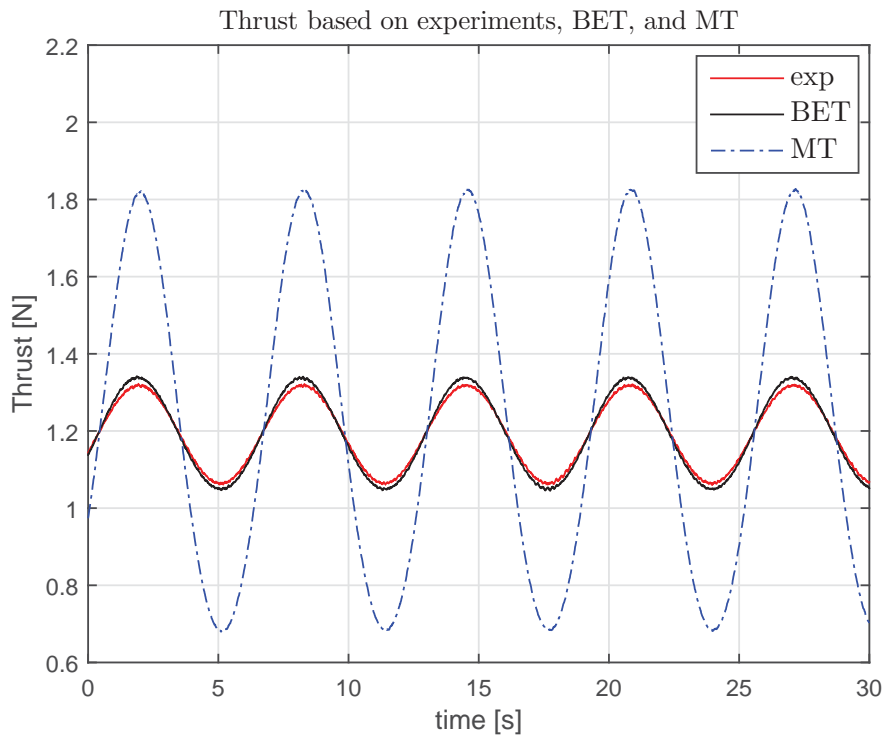


Figure 5.7: Thrust calculations with BET and MT and the thrust experimentally determined by Jeurgens for the 3D trajectory described in (2.4)

5.2.5 Non-uniform inflow

As mentioned in the previous section, Assumption 5.2.1 (v) might hold in hover and axial flight, however, in other flight cases, such as forward flight, the induced velocity has a non uniform distribution over the rotor disk. Glauert, proposed a first harmonic non uniform inflow distribution, which is extended by Payne [29]

$$\begin{aligned}\lambda &= \lambda_0 \left(1 + K_c \frac{r}{R} \cos(\psi) + K_s \frac{r}{R} \sin(\psi) \right) \\ &= \lambda_0 + \lambda_c \frac{r}{R} \cos(\psi) + \lambda_s \frac{r}{R} \sin(\psi).\end{aligned}\quad (5.71)$$

The coefficients K_c and K_s are functions of the advance ratio, μ , since they must be zero at hover. As mentioned in the literature review of Chen [29], Section 4.1.1, Cheeseman and Haddow concluded that the longitudinal and lateral inflow coefficients of Pitt and Peters, and Drees compared best to the experimental data. Based on their conclusion the model of Pitt and Peters is followed, with

$$\begin{aligned}K_c &= \frac{15\pi}{32} \tan\left(\frac{\chi}{2}\right) \\ K_s &= 0,\end{aligned}\quad (5.72)$$

with the wake skew angle defined as

$$\chi = \frac{\mu}{\lambda}.\quad (5.73)$$

So far, a uniform inflow has been used. The thrust, drag and side force must be adapted to account for the non-uniform inflow. The additional contribution of the non-uniform inflow for the thrust coefficient is given by [12]

$$\begin{aligned}C_T &= \frac{\sigma a}{4\pi} \int_0^1 \int_0^{2\pi} (-\Delta\lambda V_T) d\psi dr \\ &= \frac{\sigma a}{2} \left(-\frac{1}{4} \lambda_s \mu \right)\end{aligned}\quad (5.74)$$

with V_T defined in (5.16) and the inflow difference, $\Delta\lambda$ given by

$$\Delta\lambda = \lambda_c \frac{r}{R} \cos(\psi) + \lambda_s \frac{r}{R} \sin(\psi).\quad (5.75)$$

Note that along the derivation the expression is averaged over the azimuth following the same procedure as in Section 5.1.2. The new thrust coefficient is defined as

$$C_T = \frac{\sigma a}{2} \left[\theta_0 \left(\frac{1}{3} + \frac{1}{2} \mu^2 \right) + \theta_{tw} \left(\frac{1}{4} + \frac{1}{4} \mu^2 \right) - \frac{1}{2} \left(\lambda_0 + \frac{1}{2} \mu \lambda_s \right) \right].\quad (5.76)$$

Using the same procedure the rotor drag and side force coefficients are [12]

$$C_{HTPP} = \frac{\sigma a}{2} \left[\frac{1}{2} \mu \lambda \left(\theta_0 + \frac{1}{2} \theta_{tw} \right) + \frac{1}{4} \mu \beta_0^2 + \frac{1}{6} \lambda_c \beta_0 + \lambda_s \left(\frac{1}{6} \theta_0 + \frac{1}{8} \theta_{tw} - \frac{1}{2} \lambda_0 \right) \right]\quad (5.77a)$$

$$C_{YTPP} = -\frac{\sigma a}{2} \left[\frac{3}{4} \mu \beta_0 \left(\theta_0 + \frac{2}{3} \theta_{tw} \right) - \frac{3}{2} \mu \beta_0 \lambda + \lambda_c \left(\frac{1}{6} \theta_0 + \frac{1}{8} \theta_{tw} - \frac{1}{2} \lambda_0 \right) - \frac{1}{6} \lambda_s \beta_0 \right].\quad (5.77b)$$

5.3 Blade flapping

Besides induced drag, blade flapping is considered to play an important role in the behavior of the quadrotor as well. Several flight maneuvers affect blade flapping, with the most important

ones being forward flight and pitch or roll maneuvers. Furthermore, based on recent studies it is chosen to follow the work of [14].

In modeling a cantilevered rotor for blade flapping, [12, 14] both state that the behavior can be estimated with a model of a hinged rotor, using an effect offset e_f to account for the bending of the blades. This offset can be derived from experiments, however, the design of the AR Drone rotor blades incorporates a rib at the hub to provide stiffness, see Figure 5.8. The rib extends into the blades and the ends might act as a fictional hinge.



Figure 5.8: Detailed view of the rotor blade at the hub. In the middle of the blade the rib which gives stiffness to the rotor hub. The rib extends into the blades and might act as a fictional hinge.

5.3.1 Forward flight

The complete equations for blade flapping in forward flight can be derived by equating the effective moments acting at the hinge. A hinge can not support a moment, therefore the sum of all moments must be zero. In the derivation it is assumed the blade motion only consists of coning and first harmonic blade flapping. This assumption ensures the centrifugal forces to lie in the plane of rotation and thereby eliminate all inertia moments from the analysis. The contribution of the centrifugal force to the moment about the hinge is given by

$$\Delta M_{CF} = -\Delta CF h, \quad (5.78)$$

with

$$\Delta CF = m(r' + e_f)\Omega^2 \Delta r, \quad (5.79)$$

and

$$h = r'b_0 + \frac{e_f}{r' + e_f}(r'\beta - r'\beta_0). \quad (5.80)$$

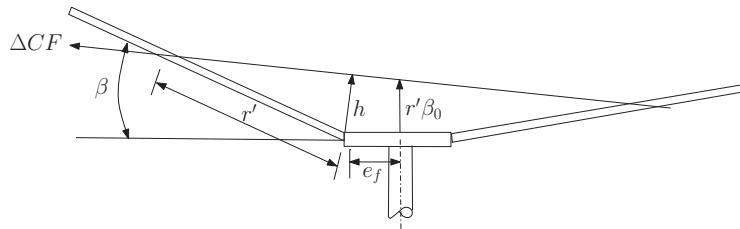


Figure 5.9: Schematic representation of the blade including the increment of the centrifugal force and the distances h , e_f , r' , [14].

Assuming only first harmonic flapping and steady state conditions the blade flapping angle, β , can be estimated with a Fourier series

$$\beta = \beta_0 - \beta_{1c} \cos(\psi) - \beta_{1s} \sin(\psi). \quad (5.81)$$

Substituting (5.81) into (5.78), results in

$$\Delta M_{CF} = -mr'(r' + e_f)\Omega^2 \left[\beta_0 - \frac{e_f}{r' + e_f}(\beta_{1c} \cos(\psi) + \beta_{1s} \sin(\psi)) \right] \Delta r. \quad (5.82)$$

Integrating out from the hinge gives the total centrifugal moment

$$M_{CF} = -\Omega^2 \left[\beta_0 \left(I_b + e_f \frac{M_b}{g} \right) - (\beta_{1c} \cos(\psi) + \beta_{1s} \sin(\psi)) e_f \frac{M_b}{g} \right]. \quad (5.83)$$

The lift generated by the blade contributes to the hinge moment as well and can be defined as

$$M_A = \int_0^{R-e} r' \frac{\rho}{2} a_0 c \alpha_{bs} V_T^2 dr', \quad (5.84)$$

where the velocity components follow from blade element theory, however, the tangential velocity is redefined to account for the effective offset

$$V_T = \Omega R \left[\frac{r' + e_f}{R} + \mu \sin(\psi) \right]. \quad (5.85)$$

Since only first harmonic flapping is considered, the moment can be written in terms of the constant, sine, and cosine terms, using trigonometric identities, after which the higher harmonics are excluded

$$M_A = M_{A_{const}} + M_{A_{sine}} \sin(\psi) + M_{A_{cosine}} \cos(\psi). \quad (5.86)$$

The blade flap angles β_0 , β_{1s} and β_{1c} can be solved using the three equations

$$M_{CF_{const}} + M_{A_{const}} + M_w = 0 \quad (5.87a)$$

$$M_{CF_{sine}} + M_{A_{sine}} = 0 \quad (5.87b)$$

$$M_{CF_{cosine}} + M_{A_{cosine}} = 0, \quad (5.87c)$$

where

$$M_w = -M_b = - \int_0^{R-e} mgr' dr'. \quad (5.88)$$

The coning angle β_0 can be derived from the constant equation and afterwards used in the sine and cosine equations to solve for β_{1s} and β_{1c} . However, a simplified coning angle is used, which expresses the coning angle in terms of the thrust constant C_T [14]

$$\beta_0 = \frac{2}{3} \gamma \frac{C_T / \sigma}{a_0} \frac{\left(1 - \frac{e_f}{R}\right)^2}{1 + \frac{1}{2} \frac{e_f}{R}}. \quad (5.89)$$

Note that in this case the definition for C_T is different than defined in (5.25a). The tangential velocity is different because of the incorporation of the effect hinge offset, furthermore, the integration is performed from the hinge offset to the tip instead of the hub, i.e.

$$C_T = \frac{\sigma a_0}{4\pi} \int_0^{R-e_f} \int_0^{2\pi} (V_T^2 \theta - V_P V_T) d\psi dr \quad (5.90a)$$

$$= (1 - e_f) \frac{\sigma a_0}{4} \left[\theta_0 \left(\frac{2}{3} + \mu^2 \right) + \theta_{tw} \left(\frac{1}{2} + \frac{\mu^2}{2} \right) + \mu \alpha_d - \lambda \right]. \quad (5.90b)$$

The blade flapping model is based on [14], therefore the thrust coefficient defined in his model is used, which is different from the definition given by [12] from which BET and MT is used. The reason why only the thrust coefficient depends on the hinge offset is because the hinge is not capable of generating a lift force, however, it is of influence in the drag and side forces.

In performing the derivation of the sine and cosine equations a discrepancy is noticed. The sine equation becomes

$$\Omega^2 \beta_{1_s} e_f \frac{M_b}{g} + \frac{\gamma I_b}{2} \Omega^2 \left(1 - \frac{e_f}{R}\right)^2 \left[\frac{2}{3} \theta_0 \mu + \frac{1}{2} \theta_{tw} \mu + \frac{\mu}{2} \left(\mu \alpha_d - \frac{v_i}{\Omega R} \right) - \beta_{1_c} \left(\frac{1}{4} - \frac{\mu^2}{8} \right) \right] = 0, \quad (5.91)$$

and the cosine equation becomes

$$\Omega^2 \beta_{1_c} e_f \frac{M_b}{g} + \frac{\gamma I_b}{2} \Omega^2 \left(1 - \frac{e_f}{R}\right)^2 \left[-\frac{\beta_0 \mu}{3} - \frac{K_c}{4} \frac{v_i}{\Omega R} + \beta_{1_s} \left(\frac{1}{4} + \frac{\mu^2}{8} \right) \right] = 0. \quad (5.92)$$

Notice the difference in the λ_i term with respect to [14], which uses a factor of $1/3$. However, following the derivation the factor should be $1/4$. Furthermore, notice the lateral inflow coefficient K_c appearing in the cosine equation, where [14] conveniently left it out because it is assumed that $K_c = 1$. The flapping angles β_{1_s} and β_{1_c} can be found by solving these two equations. In the derivation [14] use the following approximations

$$e \frac{M_b}{I_b g} = \frac{\frac{3}{2} \frac{e_f}{R}}{1 - \frac{e_f}{R}} \quad (5.93a)$$

$$\frac{\nu_1}{\Omega R} = \frac{C_T}{\sigma} \frac{\sigma}{2\mu}. \quad (5.93b)$$

Equation (5.93b) equates the induced velocity equivalent to the thrust constant divided by the advance ration. This substitution, however, is only valid with higher advance ratios, [12, 13], and leads to an over estimation of the flapping angles in the lower advance ratios.

The equation for the longitudinal and lateral flapping are:

$$\beta_{1_c f} = \frac{\frac{8}{3} \theta_0 \mu + 2 \theta_{tw} \mu + 2 \mu (\mu \alpha_d - \lambda)}{\left(1 - \frac{\mu^2}{2}\right) + \frac{144 \left(\frac{e_f}{R}\right)^2}{\gamma^2 \left(1 - \frac{e_f}{R}\right)^6 \left(1 + \frac{\mu^2}{2}\right)}} + \frac{12 \left(\frac{e_f}{R}\right)}{\gamma \left(1 - \frac{e_f}{R}\right)^3 \left(1 + \frac{\mu^2}{2}\right)} \left(\frac{\frac{8}{9} C_T / \sigma \frac{\mu \gamma}{a_0} \frac{\left(1 - \frac{e_f}{R}\right)^2}{1 + \frac{3e}{2R}} + K_c \lambda}{\left(1 - \frac{\mu^2}{2}\right) + \frac{144 \left(\frac{e_f}{R}\right)^2}{\gamma^2 \left(1 - \frac{e_f}{R}\right)^6 \left(1 + \frac{\mu^2}{2}\right)}} \right) \quad (5.94a)$$

$$\beta_{1_s f} = \frac{\frac{8}{9} C_T / \sigma \frac{\mu \gamma}{a_0} \frac{\left(1 - \frac{e_f}{R}\right)^2}{1 + \frac{3e}{2R}} + K_c \lambda}{\left(1 + \frac{\mu^2}{2}\right) + \frac{144 \left(\frac{e_f}{R}\right)^2}{\gamma^2 \left(1 - \frac{e_f}{R}\right)^6 \left(1 - \frac{\mu^2}{2}\right)}} - \frac{12 \left(\frac{e_f}{R}\right)}{\gamma \left(1 - \frac{e_f}{R}\right)^3 \left(1 - \frac{\mu^2}{2}\right)} \left(\frac{\frac{8}{3} \theta_0 \mu + 2 \theta_{tw} \mu + 2 \mu (\mu \alpha_d - \lambda)}{\left(1 + \frac{\mu^2}{2}\right) + \frac{144 \left(\frac{e_f}{R}\right)^2}{\gamma^2 \left(1 - \frac{e_f}{R}\right)^6 \left(1 - \frac{\mu^2}{2}\right)}} \right). \quad (5.94b)$$

Notice the difference, with respect to [14], in the last term of $\beta_{1_c f}$ and the first term in $\beta_{1_s f}$ and the minus sign in front of the second term in $\beta_{1_s f}$. Furthermore, notice the appearance of K_c in front of λ . Using the definitions of K_c and K_s of Pitt and Peters, $K_s = 0$ and therefore can be left out the equation.

In [14] these relations are simplified by neglecting the second term in each denominator, assuming it is much smaller with respect to the first terms. This assumption may be accurate in case of helicopters, for quadrotors this term can not be neglected. Compared to helicopters the effective hinge offset of the rotor blade of the AR Drone is a larger part of the entire blade. Furthermore, the Lock number for helicopters is in the range of 5-8 [12, 14], for the quadrotor this is about 2.5.

The blade flapping model derived by [14] is based on a inertial frame. The angular velocities are compensated for by [14], however, angular and rectilinear accelerations are not accounted for.

Assumption 5.3.1. *The following assumptions are used in the deriving the flapping model*

- (i) *The aerodynamic forces are considered to act from the hinge to the tip*
- (ii) *The reverse flow region is ignored*
- (iii) *The airfoil lift characteristics are linear and free of stall and compressibility effects*
- (iv) *The blade motion consists of only coning and first harmonic flapping*
- (v) *The inflow and blade flap angles are small*
- (vi) *The blade geometry can be described by linear twist*
- (vii) *The forward flight conditions are steady*
- (viii) *The reference frame is a wind axis NED inertial frame*

5.3.2 Angular velocity blade flapping

Beside the effect of forward flight on blade flapping, pitch and roll maneuvers influence the flapping behavior as well. The moment equation at the hinge becomes

$$M_{CF} + M_A + M_w + M_{gyro} = 0 \quad (5.95)$$

The extra term in the equation, with respect to forward flight, is due to the gyroscopic effects of the rotor. The increment of the moment due to the gyroscopic effect can be defined as:

$$\Delta M_{gyro} = r(-\alpha_{gyro}m)dr' \quad (5.96)$$

The vertical velocity at a blade element exists of four components, two due to the pitch and roll rates without rotation, and two due to rotation on a constantly pitching and rolling disc [14]

$$V_{gyro} = -qr \cos(\psi) - pr \sin(\psi) + \Omega r \sin(\psi)qdt - \Omega r \cos(\psi)pdt \quad (5.97)$$

from which the acceleration can be derived

$$\alpha_{gyro} = 2qr\Omega \sin(\psi) - 2pr\Omega \cos(\psi). \quad (5.98)$$

The resultant moment is

$$M_{gyro} = \int_0^{(R-e)} (r' + e)m[2q(r' + e)\Omega \sin(\psi) - 2p(r' + e)\Omega \cos(\psi)]dr' \quad (5.99)$$

from which the sine and cosine components can be derived

$$M_{gyro_{sine}} = -2q\Omega I_b \quad (5.100a)$$

$$M_{gyro_{cosine}} = 2p\Omega I_b. \quad (5.100b)$$

The definitions for the centrifugal moment and the weight moment are the same as in forward flight. The contribution of the aerodynamic moment to the hinge moment is given in (5.86). Because the forward flight case is already taken into account only the change in angle of attack caused by the angular rates needs to be considered. The results can be superimposed on the flapping due to steady forward flight. The local angle of attack is defined as [14]

$$\alpha = \frac{V_{Par}}{V_{Tar}} \quad (5.101)$$

with

$$\begin{aligned} V_{Par} &= (r' + e)(q \cos(\psi) + p \sin(\psi)) - r\Omega(b_{1c} \sin(\psi) - b_{1s} \cos(\psi)) + \\ &\quad V(b_{1c} \cos(\psi) + b_{1s} \sin(\psi)) \cos(\psi) \\ V_{Tar} &= \Omega(r' + e) + V \sin(\psi). \end{aligned} \quad (5.102)$$

Substituting this in the equation for the aerodynamic moment (5.86) and neglecting the higher harmonics results in [14]

$$M_A = \frac{\rho}{8} a_0 c (\Omega R)^2 \left(1 - \frac{e_f}{R}\right)^2 R^2 \left\{ \left[\frac{p}{\omega} - \left(1 - \frac{\mu^2}{2}\right) b_{1c} \right] \sin(\psi) + \left[\frac{q}{\omega} + \left(1 + \frac{\mu^2}{2}\right) b_{1s} \right] \cos(\psi) \right\}. \quad (5.103)$$

The total moment about the hinge becomes

$$M_{sine} = \Omega^2 e \frac{M b}{g} b_{1s} + \frac{\rho}{8} a_0 c (\Omega R)^2 \left(1 - \frac{e_f}{R}\right)^2 R^2 \left[\frac{p}{\Omega} - \left(1 - \frac{\mu^2}{2}\right) b_{1c} \right] - 2q\Omega I_b \quad (5.104a)$$

$$M_{cosine} = \Omega^2 e \frac{M b}{g} b_{1c} + \frac{\rho}{8} a_0 c (\Omega R)^2 \left(1 - \frac{e_f}{R}\right)^2 R^2 \left[\frac{q}{\Omega} + \left(1 + \frac{\mu^2}{2}\right) b_{1s} \right] + 2p\Omega I_b. \quad (5.104b)$$

These two equations can be solved simultaneously to derive the longitudinal and lateral flapping angle due to the angular velocities

$$\beta_{1ca} = \frac{\frac{p}{\Omega} - \frac{\frac{16}{\gamma} \frac{q}{\Omega}}{\left(1 - \frac{e_f}{R}\right)^2}}{\left(1 - \frac{\mu^2}{2}\right) + \frac{144 \left(\frac{e_f}{R}\right)^2}{\gamma^2 \left(1 - \frac{e_f}{R}\right)^6 \left(1 + \frac{\mu^2}{2}\right)}} + \frac{\frac{\frac{12}{\gamma} \frac{e_f}{R}}{\left(1 - \frac{e_f}{R}\right)^3} \left[-\frac{q}{\Omega} - \frac{\frac{16}{\gamma} \frac{p}{\Omega}}{\left(1 - \frac{e_f}{R}\right)^2} \right]}{\left(1 - \frac{\mu^4}{4}\right) + \frac{144 \left(\frac{e_f}{R}\right)^2}{\gamma^2 \left(1 - \frac{e_f}{R}\right)^6}} \quad (5.105a)$$

$$\beta_{1sa} = \frac{-\frac{q}{\Omega} - \frac{\frac{16}{\gamma} \frac{p}{\Omega}}{\left(1 - \frac{e_f}{R}\right)^2}}{\left(1 + \frac{\mu^2}{2}\right) + \frac{144 \left(\frac{e_f}{R}\right)^2}{\gamma^2 \left(1 - \frac{e_f}{R}\right)^6 \left(1 - \frac{\mu^2}{2}\right)}} + \frac{\frac{\frac{12}{\gamma} \frac{e_f}{R}}{\left(1 - \frac{e_f}{R}\right)^3} \left[-\frac{p}{\Omega} + \frac{\frac{16}{\gamma} \frac{q}{\Omega}}{\left(1 - \frac{e_f}{R}\right)^2} \right]}{\left(1 - \frac{\mu^4}{4}\right) + \frac{144 \left(\frac{e_f}{R}\right)^2}{\gamma^2 \left(1 - \frac{e_f}{R}\right)^6}}. \quad (5.105b)$$

As in the case of forward flight [14] simplifies these expression by neglecting the second term in the denominator, which might hold for helicopters, however, for quadrotors this term should be included.

5.4 Extended model

The forces on the rotor hub are analyzed using Blade element theory. It is shown that the rotor experiences a rotor drag and side forces because of the induced drag of the rotor blades. Furthermore, blade flapping generates also drag forces in the rotor plane. The model derived by [5] needs to be updated to include the behavior of blade flapping and induced drag. To incorporate the rotor aerodynamics in the quadrotor dynamics, an extended model is defined based on [15], extending the simplified dynamics of (2.2).

$$\dot{\rho} = R\nu \quad (5.106a)$$

$$\dot{\nu} = -S(\omega)\nu + gR^T e_3 - \frac{1}{m} \left(\sum_{i=1}^n T_i \right) \quad (5.106b)$$

$$\dot{R} = RS(\omega) \quad (5.106c)$$

$$J\dot{\omega} = S(J\omega)\omega + \tau_3 + \sum_{i=1}^n M_i \quad (5.106d)$$

$$T_i = C_{T_i} \rho A (\Omega_i R)^2 \begin{pmatrix} s\beta_{1ci} \\ c\beta_{1ci} s\beta_{1si} \\ c\beta_{1ci} c\beta_{1si} \end{pmatrix} + R_{cb} R_{TH} \begin{bmatrix} C_{H_i} \\ C_{Y_i} \\ 0 \end{bmatrix} \rho A (\Omega_i R)^2 \quad (5.106e)$$

$$M_i = D_i \times T_i, \quad (5.106f)$$

where n is the number of rotors, $s\{\cdot\}$ and $c\{\cdot\}$ are the sine and cosine functions, $S(\omega)$ is a skew symmetric matrix, defined as in (2.3). The torque about the b_3 axis of the body fixed frame, τ_3 , is defined as in (2.1), and D_i the distance vector from the center of mass to each rotor

$$\begin{aligned} D_1 &= [l \quad -l \quad -h]^T \\ D_2 &= [l \quad l \quad -h]^T \\ D_3 &= [-l \quad l \quad -h]^T \\ D_4 &= [-l \quad -l \quad -h]^T. \end{aligned} \quad (5.107)$$

The inertia matrix J is defined as

$$J = \begin{bmatrix} J_{xx} & 0 & 0 \\ 0 & J_{yy} & 0 \\ 0 & 0 & J_{zz} \end{bmatrix}.$$

The force coefficients are defined as

$$C_T = \kappa_T \frac{\sigma a_0}{2} \left[\theta_0 \left(\frac{1}{3} + \frac{1}{2} \mu^2 \right) + \theta_{tw} \left(\frac{1}{4} + \frac{1}{4} \mu^2 \right) - \frac{1}{2} \lambda \right] \quad (5.108a)$$

$$C_H = \frac{\sigma a_0}{2} \left[\frac{1}{2} \mu \lambda \left(\theta_0 + \frac{1}{2} \theta_{tw} \right) + \frac{1}{4} \mu \beta_0^2 \right] \quad (5.108b)$$

$$C_Y = -\frac{\sigma a_0}{2} \left[\frac{3}{4} \mu \beta_0 \left(\theta_0 + \frac{2}{3} \theta_{tw} \right) - \frac{3}{2} \mu \beta_0 \lambda \right], \quad (5.108c)$$

with λ the inflow ratio

$$\lambda = \mu_c + \mu \tan(\alpha_d) + \lambda_i, \quad (5.109)$$

where μ is defined as in (5.111c) and

$$\mu_c = \frac{n\nu_{r(3)i}}{\Omega R}, \quad (5.110)$$

with ν_{r_i} defined in (5.111b).

The quadrotor's front is not necessarily aligned with the direction of motion, hence the flapping axes are not aligned with the front of the quadrotor. Therefore, the body fixed reference frame, \mathcal{C} , is used, which is aligned with the quadrotor's flight direction. The flapping of the rotor is first calculated in this rotor frame and then transformed into body fixed, \mathcal{B} , coordinates using

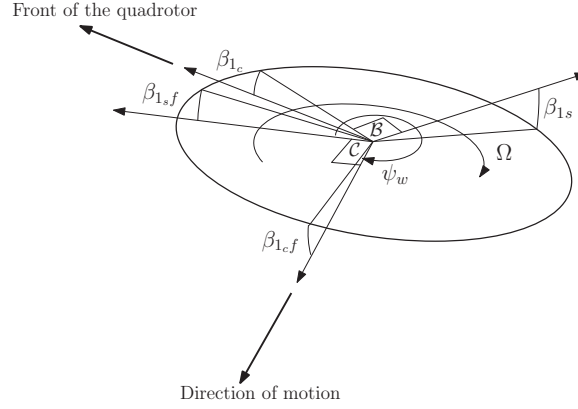


Figure 5.10: Blade flapping angles in the rotor frame, $\beta_{1_{c}fi}$ and $\beta_{1_{s}fi}$, and in the body fixed frame, $\beta_{1_{s}i}$ and $\beta_{1_{c}i}$ [15]

the rotation matrix R_{bc} as defined in (3.5). Note that this also holds for the force coefficients C_H , C_Y , and the inflow ratio λ . They are all derived with respect to the body fixed reference frame \mathcal{C} .

In order to determine the flapping angles $\beta_{1_{s}i}$ and $\beta_{1_{c}i}$, first the advance ratio μ_i and azimuthal direction ψ_i of the rotors are calculated [15]

$$\nu_{ri} = \nu + \Omega \times D_i \quad (5.111a)$$

$$\mu_i = \frac{\|\nu_{r(1,2)i}\|}{\Omega_i R} \quad (5.111b)$$

$$\psi_{wi} = \tan^{-1} \left(\frac{\nu_{r(2)i}}{\nu_{r(1)i}} \right), \quad (5.111c)$$

with $\nu_{r(n)i}$ the n^{th} element of the i^{th} rotors velocity, which is based on both the linear and angular velocity of the quadrotor. The local flapping angles are then transferred into body coordinates, using the rotation matrix R_{cb} , see (3.5), to derive the flapping angles due to the motion of the quadrotor

$$\begin{bmatrix} \beta_{1_{c}i} \\ \beta_{1_{s}i} \end{bmatrix} = R_{cb} \begin{bmatrix} \beta_{1_{c}fi} \\ \beta_{1_{s}fi} \end{bmatrix}, \quad (5.112)$$

Note that the rotation matrix, in this case, is a modified version because only the in plane components are taken into account. The pitch and roll rates of the quadrotor itself also affect the blade flapping behavior as shown in Section 5.3.2. Therefore, the components of the flapping angles due to the pitch and roll rates of the quadrotor are added to those of the body fixed frame [14, 64].

$$\beta_{1_{c}i} = \beta_{1_{c}i} + \beta_{1_{c}ai} \quad (5.113a)$$

$$\beta_{1_{s}i} = \beta_{1_{s}i} + \beta_{1_{s}ai} \quad (5.113b)$$

The blade flapping angles due to forward flight $\beta_{1_{c}fi}$ and $\beta_{1_{s}fi}$ are defined in (5.94) and the blade flapping angles due to angular velocities $\beta_{1_{c}ai}$ and $\beta_{1_{s}ai}$ are defined in (5.105).

5.5 Simulation results

From the experiments performed by [4] and [5] it can be concluded that the tracking performance for fast time-varying trajectories is insufficient. The revised controller by [7] improved the

tracking performance, however, still a significant mismatch between the reference and actual trajectory existed, see Section 2.4. In this section the improvement of the extended model with respect to the rigid body model of [5] (2.2) is investigated in simulation.

In [4] a simulation environment is provided, in which the rigid body dynamics of (2.2), the quadrotor dynamics, the observers, and the controller designed by [5] are incorporated. The simulation results of this model showed that the controller was perfectly able to track the reference trajectory with the AR Drone. However, the experimental results showed otherwise, see Section 2.4. To investigate the improvement of the new extended model, how close it can estimate the actual behavior of the quadrotor, the new extended model is incorporated into the simulation environment. This should lead to simulation results which are more closely to the experimental results. Note that the improved controller of [7] is used in the simulation. Therefore, the simulation results should be compared with the experiments from Section 2.4. The ultimate goal is to improve the controller such that in reality the quadrotor is able to track the reference. This improvement is not performed, yet, and is a recommendation for future work.

Figure 5.11 shows the simulation results of the rigid body model (black) and the new extended model (blue), together with the experimental measurements (red), for the three-dimensional circular reference trajectory parametrized as

$$\rho_r = [\cos(a_t t) \quad \sin(a_t t) \quad 1.5 + \sin(a_t t)]^T, \quad (5.114)$$

with a_t a time constant and $a_t = 1$. Note that in all figures below the reference is left out for clarity reasons, the reference is almost the same as the rigid body simulation results.

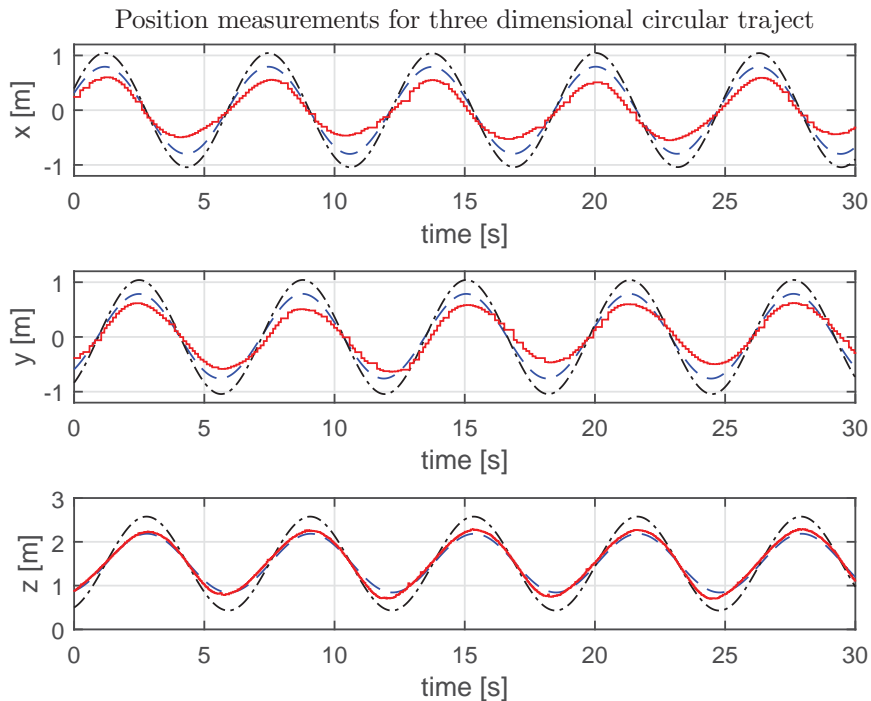


Figure 5.11: Position measurements of the new extended model in which the induced and blade flapping drag forces are included. In black the old simulation result based on the model of (2.2), in blue the simulation results of the new model and in red the measurements of the experiment as described in Section 2.4

The simulation results of Figure 5.11 show improvement in the position estimation of the extended model. Compared to the experimental results of Section 2.4, the new model is able to estimate the z -dynamics closely. Furthermore, the position estimations in x and y -direction are improved as well, however, they are not as accurate as the z -direction. The $x - y$ plane simulation results of the new model are almost 50% more close to the experimental results than the simulation results of the old rigid body model.

Investigating the performance of the new model in two-dimensional trajectories leads to the results of figures 5.12 and 5.13. Figure 5.12 shows the simulations results of tracking a two-dimensional circular reference trajectory in the $x - y$ plane, which is parametrized as

$$\rho_r = [\cos(a_t t) \quad \sin(a_t t) \quad 1.0]^T. \quad (5.115)$$

In Figure 5.13 the motion is only in the z direction and the reference trajectory is parametrized as

$$\rho_r = [0 \quad 0 \quad 1.5 + \sin(a_t t)]^T. \quad (5.116)$$

In Both experiments $a_t = 1$. Notice the similarities between the experimental results of the three and two-dimensional circular trajectories. The x and y -dynamics of both cases are almost the same, which might suggest that the in and out of plane dynamics are decoupled. From Figure 5.12 it can be seen that simulation results of the new extended model are more close to the experimental results than the rigid body model. As in the case of the three dimensional trajectory, the new model is almost 50% more accurate than the old model when compared to the experimental results. Because the z -dynamics seems to be decoupled from the in plane motion, the difference between the simulation results of the new model and the experimental results may be caused by the limitations of the blade flapping and inflow model. From both phenomena it is know that they induce drag forces in the $x - y$ plane, therefore, not being able to estimate the behavior of blade flapping, inflow, and wake accurately may lead to underestimation of the drag forces.

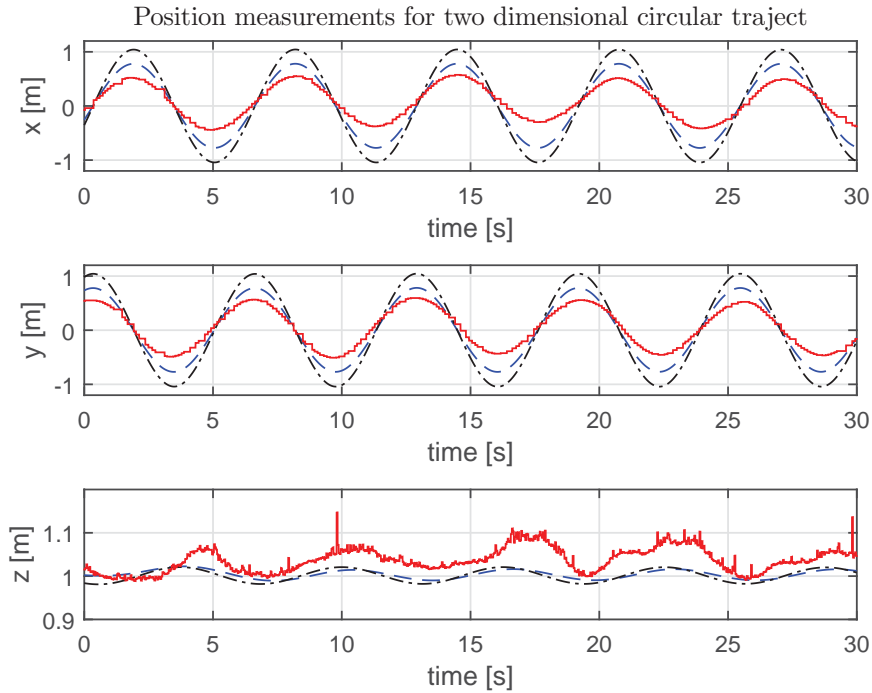


Figure 5.12: Position measurements for a two dimensional circular trajectory. Black indicates the old simulation result based on the model of (2.2), blue the simulation results of the extended model, and red the experiment results

In z -direction, shown in Figure 5.13, the simulation results show a much better performance for the extended model than the rigid body model. The amplitude of the trajectory in the new model is reduced compared to the old model and is almost similar to the experimental results.

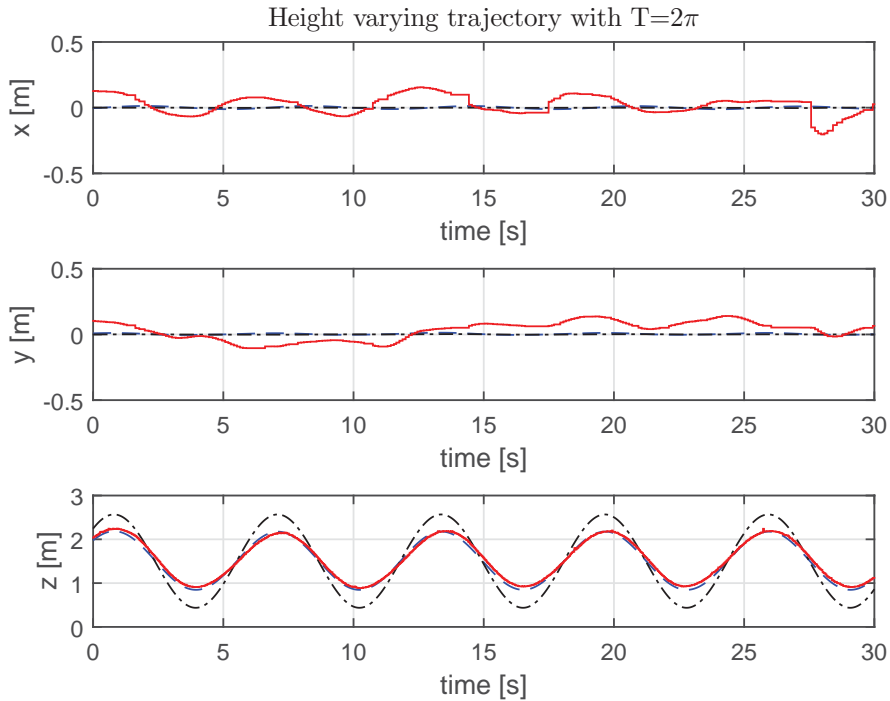


Figure 5.13: Position measurements of the new extended model for a varying height trajectory with $T = 2\pi$. In black the old simulation result, in blue the simulation results of the new model, and in red the measurements of the experiment

In Figure 5.14 the experimental result of a height varying trajectories of Section 2.4 is shown again, because some important observations need to be made. The trajectory is described by (5.116) with $a_t = 2$. In the experimental results the quadrotor seems not to be affected by any turbulence, which is expected according to helicopter theory, see Chapter 3. According to Section 3.4 the boundaries of the vortex ring state are at $1/4v_h \leq -V_c \leq 2v_h$, which for the AR Drone are $1 \leq -V_c \leq 8$. In the experiment of Figure 5.14 the lower boundary should be crossed, however, disturbances due to heavy turbulence are not noticed. The maximum and minimum heights are not constant, however, this is most probably due to the quadrotor lacking in time. The rotors are not able to deliver the thrust required for such a fast varying trajectory, hence the limits of the quadrotor are reached. Because of reaching the limits of the AR Drone further experiments are not performed, however, it would be interesting to investigate when and if the quadrotor enters the vortex ring state.

5.6 Concluding remarks

Blade element theory derives from the blade forces the thrust force acting on the entire rotor and the drag and side forces acting on the rotor hub. Blade element theory is not capable of calculating the induced velocity, therefore, momentum theory extended with a first order non-uniform inflow distribution is used. The non-uniform inflow coefficients are based on the work of Pitt and Peters [38,39]. The out of plane movement of the rotor blades causes drag and

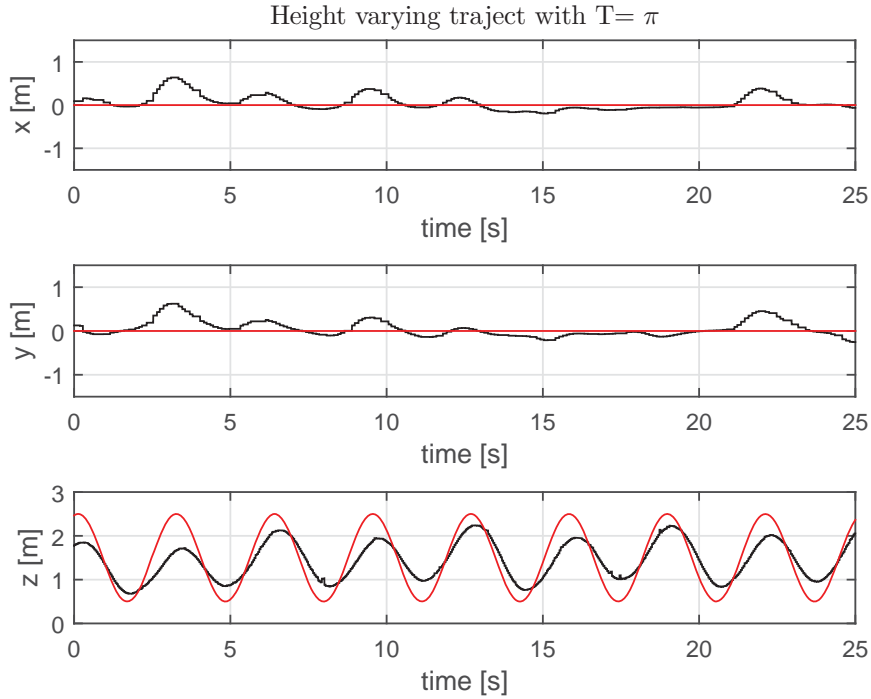


Figure 5.14: Representation of a height varying trajectory in each separate direction with the experimental results in red, the new simulation results in blue, and the old results in black. The old results are almost similar to the reference trajectory. The trajectory is described in (5.116) with $a_t = 2$, i.e. $T = \pi$

side forces acting on the rotor hub and are modeled using the blade flapping model of Prouty. These aerodynamic influences are incorporated into an extended model, which is based on the rigid body model of van der Eijnden (2.2).

In the experimental results it is noticed that the quadrotor does not seem to be influenced by any turbulence. According to helicopter literature the quadrotor should enter the VRS, in which heavy turbulence affects the control of the helicopter. In none of the experiments this behavior is noticed. It would be worth looking into this phenomena more closely, however, as explained the AR Drone reached its limits in the last height varying experiment and therefore is insufficient to perform the required tests.

The performance of the new quadrotor model has been investigated in simulations and is compared with the old simulation results and the experimental results of Section 2.4. The new model has been implemented into the simulation environment made by Jeurgens, while the controller designed by van der Eijnden and Lefeber [7] has been used. The new model is tested with three cases, a three dimensional circular trajectory, a two dimensional circular trajectory, and a height varying trajectory. Compared to the experimental results, the simulation results of the new extended model show a good performance in estimating the z -dynamics, and show an improvement in estimating the x and y -positions. The in plane diameter difference between the old rigid body model simulations and the experiments is about 1m. The difference between simulations of the new model and the experiments is about 0.5m. Comparing the experimental results of the three-dimensional with the two-dimensional trajectory shows that the z -dynamics might not have any influence on the in plane $x - y$ dynamics. This suggests that these two dynamics are decoupled. Therefore, the difference in the $x - y$ plane between the simulation results and the experimental results most probably is due to limitations in the blade flapping and inflow model, from which it is known they induce drag forces in the $x - y$ plane.

Chapter 6

Conclusions and Recommendations

6.1 Conclusions

This thesis is part of a larger research project on cooperation of drones capable of vertical take of and landing. Previous work in this project resulted in a quadrotor capable of tracking a trajectory. However, whereas the tracking performance for slow time-varying trajectories is satisfactory the tracking performance for fast time-varying trajectories is insufficient. To deploy multiple drones in cooperation accuracy in following the trajectory is of high importance. Therefore, adjustments to the previous work is needed to improve the tracking performance.

After implementing an improved controller, designed by [7], part of the tracking accuracy had been solved, however, the large position error between the reference and actual path still existed. Additional experiments have been performed to determine the nature of the tracking problem. Based on this data it is concluded that the rigid body model, which neglects aerodynamic forces, is not capable of capturing the quadrotor's behavior accurately. Combined with recent studies [9,10] blade flapping and induced inflow are identified as the possible sources influencing the tracking performance. Both inflow and blade flapping generate drag forces in the $b_1 - b_2$ plane of the quadrotor's body fixed frame and can not be solved with high gain control [10].

Based on the capabilities of the processor of the AR Drone and the work of [9,10], the most simple inflow theories, Blade element and Momentum theory, and the blade flapping model of [14] are implemented. The axial and forward flight cases of BET and MT are combined to allow for three-dimensional trajectories. Furthermore, the blade flapping model of [14] is adjusted to incorporate inflow coefficients and remove the assumptions of high speed forward flight.

An extended model is developed to include those aerodynamics into the rigid body dynamics of [5]. This extended model has been implemented into the simulation environment made by [4], together with the controller designed by [7]. The simulation results show that the extended model has a good performance in estimating the z -dynamics when compared to the experiments. The performance in estimating the x and y -positions has increased significantly compared to the simulation results of the rigid body model. The new model is capable of estimating the actual positions almost 50% more accurate than the old model. The extended model is thus capable of explaining roughly half the diameter difference between the simulation results of the old model and the experiments.

Comparing the experimental results of the three-dimensional with the two-dimensional trajectory shows that the x and y -dynamics are almost the same, which suggests that the z -dynamics and the in plane $x - y$ dynamics might be decoupled. Therefore, the difference in the $x - y$ plane between the simulation results of the new extended model and the experimental results, most probably is due to limitations in the blade flapping and inflow model. The inflow model does not capture the wake behavior under the rotors. It is known that these dynamics play an important part in the rotor dynamics, and consequently in the quadrotor dynamics. Furthermore, the inflow is based on a first order inflow variation, and only capable of partially capturing the inflow behavior. Higher order inflow variations are needed to fully describe the inflow behavior. Additionally, the inflow coefficients based on the work of Pitt and Peters are basic estimates and not able to capture the inflow completely. Momentum and blade element theory are both static inflow models, which assume the flow variations to be instantaneously, and only hold for steady forward or axial flight and thereby neglect the quadrotor's constant acceleration and deceleration necessary for following a trajectory.

The goal of this thesis was to improve the tracking performance by improving the quadrotor's dynamical model and redesign the controller to account for the new dynamics. For the dynamics a new extended model is introduced, which is able to estimate the z -dynamics sufficiently in simulations, and explains roughly half the in plane diameter reduction shown in experiments. However, the new model is not valid for all descent velocities, i.e. the descent velocities in which the quadrotor enters the vortex ring state. The second sub-objective of implementing the new dynamics into the controller was not achieved due to time limitations.

6.2 Recommendations

The current model based on BET and MT is based on conservation laws derived with respect to an inertial frame. Improvements can be made by removing the restrictions of an inertial frame. Several BET implementations calculate the forces per blade section and sum these to obtain the rotor forces. It would be worth investigating if this method is more accurate than the method of integration used in this thesis. One of the limitations of BET and MT is that these theories are not valid in the vortex ring state. In the experiments it is noticed that the quadrotor does not enter the vortex ring state. It would be worth investigating if the quadrotor enters the vortex ring state and at which descent rate. Furthermore, the data of Castles and Gray [63], see Figure 5.5, suggests that a relationship may exist between the induced and descent velocity in the vortex ring state. To make the extended model valid for all flight cases it would be worth investigating if such a relation can be derived for a quadrotor.

Blade flapping is incorporated based on the model of [14], which uses a hinged rotor with an effect hinge offset to account for the bending of the cantilevered rotor blades. Furthermore, [14] assumes steady state conditions in which a Fourier series can estimate the blade flap angle. Developing a rotor model based on aeroelastic deformation and removing the assumption of steady state conditions might improve the blade flap angle estimation.

Blade element and Momentum theory are both static inflow models. Dynamic inflow models are an improvement on the static inflow models in having a time dependent reaction on flow disruptions. Furthermore, dynamic inflow models are based on inflow variations, where in momentum theory inflow variation is predicted using additional inflow coefficients. Wake modeling can be included via the methods of [41] or [45], however, these methods have their limitations as well. Free vortex theory would be the most promising method because it describes both the inflow and the wake in a detailed fashion, and is able to predict the influence of the wake on the rotor

more accurately. Furthermore, vortex theory is also valid in the vortex ring state. However, a disadvantage of this method is that it can become rapidly computationally expensive. It would be worth investigating, in simulations, the improvements dynamic inflow models and or vortex theory can make compared to the new extended model and how complex the models need to be to match simulation with experiments. Because of the limitations of the AR Drone's CPU, simplified versions, can be developed to include the dynamics into the controller. Another approach can be to investigate the wake behavior with wind tunnel tests. From the test results it may become clear which rotor aerodynamics are important and should be included in the quadrotor model.

In [57] a Fast Free Wake method is developed which is capable of real time simulation on a desktop pc with margin for other simulations. The accuracy of the method is adjustable by including more or less vortex rings. It would be worth investigating how many vortex rings need to be included to accurately capture the whole rotor dynamics and if implementing this model on the CPU of the AR Drone is achievable.

A completely different solution for solving the difference between the reference trajectory and the actual trajectory is in the area of learning controllers. An online learning algorithm can be deployed to estimate the drag forces and let the actual trajectory converge to the reference trajectory. The new extended model can provide a simulation environment in which the learning algorithm can be tested.

Bibliography

- [1] P. Tripicchio, M. Satler, G. Dabisias, E. Ruffaldi, and C. A. Avizzano, “Towards smart farming and sustainable agriculture with drones,” in *proc. of the 2015 International Conference on Intelligent Environments*, pp. 140–143, July 2015.
- [2] L. Apvrille, T. J. Tanzi, and J.-L. Dugelay, “Autonomous drones for assisting rescue services within the context of natural disasters,” in *URSI GASS 2014, General Assembly and Scientific Symposium, 2014 XXXIth URSI, 16-23 August 2014, Beijing, China*, 2014.
- [3] T. Lee, K. Sreenath, and V. Kumar, “Geometric control of cooperating multiple quadrotor UAVs with a suspended payload,” in *IEEE Conference on Decision and Control (CDC)*, (Florence, Italy), pp. 5510–5515, Dec. 2013.
- [4] N. L. M. Jeurgens, “Identification and control implementation of an AR.Drone 2.0,” master’s thesis [DC report, 2017.013], Eindhoven University of Technology, Dynamics and Control Group, Department of Mechanical Engineering, Eindhoven, the Netherlands, January 2017.
- [5] S. J. A. M. van der Eijnden, “Cascade based tracking control of quadrotors,” master’s thesis [DC report, 2017.012], Eindhoven University of Technology, Dynamics and Control Group, Department of Mechanical Engineering, Eindhoven, the Netherlands, January 2017.
- [6] S. Bouabdallah, *Design and Control of Quadrotors with application to autonomous flying*. Phd thesis microtechnique report, 3727 (2007), ÉCOLE POLYTECHNIQUE FÉDÉRALE DE LAUSANNE, 2007.
- [7] E. Lefeber, S. J. A. M. van der Eijnden, and H. Nijmeijer, “Almost global tracking control of a quadrotor uav on $se(3)$,” in *56th IEEE Conference on Decision and Control, Melbourne, Australia, 2017*, IEEE, 2017.
- [8] B. C. M. van Aert, “Control and coordination algorithms for autonomous multi-agent quadrotor systems,” master’s thesis [CST report 2016.070], Eindhoven University of Technology, Control Systems Technology Group, Department of Mechanical Engineering, Eindhoven, the Netherlands, July 2016.
- [9] M. Bangura, *Aerodynamics and Control of Quadrotors*. PhD thesis, College of Engineering and Computer Science, The Australian National University, 2017.
- [10] S. Omari, M.-D. Hua, G. Ducard, and T. Hamel, “Nonlinear control of VTOL UAVs incorporating flapping dynamics,” in *proc of the 2013 International Conference on Intelligent Robots and Systems*, pp. 2419–2425, IEEE, 2013.
- [11] R. Mahony, V. Kumar, and P. Corke, “Multirotor aerial vehicles: Modeling, estimation, and control of quadrotor,” *IEEE Robotics Automation Magazine*, vol. 19, pp. 20–32, Sept 2012.
- [12] W. Johnson, *Helicopter theory*. Dover publications, inc, 1980.

- [13] J. Leishman, *Principles of Helicopter Aerodynamics*. Cambridge University press, 2002.
- [14] R. W. Prouty, *Helicopter performance, stability, and control*. Malabar, Fla. : Krieger Pub, 2005.
- [15] P. Pounds, R. Mahony, and P. Corke, “Modelling and control of a large quadrotor robot,” *Control Engineering Practice*, vol. 18, no. 7, pp. 691 – 699, 2010.
- [16] G. M. Hoffmann, H. Huang, S. L. Wasl, and E. C. J. Tomlin, “Quadrotor helicopter flight dynamics and control: Theory and experiment,” in *proc. of the AIAA Guidance, Navigation, and Control Conference*, 2007.
- [17] “Aerodynamic forces on airfoils.” <http://engineering.purdue.edu/~mark/puthesis>.
- [18] A. Bramwell, G. Done, and D. Balmford, *Bramwell’s Helicopter Dynamics*. AIAA Butterworth-Heinemann, 2001.
- [19] R. GRAY, *On the Motion of the Helical Vortex Shed from a Single-bladed Hovering Model Helicopter Rotor and Its Application to the Calculation of the Spanwise Aerodynamic Loading*. Reports, Defense Technical Information Center, 1955.
- [20] R. GRAY, *An Aerodynamic Analysis of a Singlebladed Rotor in Hovering and Low-speed Forward Flight as Determined from Smoke Studies of the Vorticity Distribution in the Wake*. Defense Technical Information Center, 1956.
- [21] e. a. Leishman JG, “Free-vortex filament methods for the analysis of helicopter rotor wakes,” *JOURNAL OF AIRCRAFT*, vol. 39, no. 5, p. 759775, 2002.
- [22] A. Landgrebe, *An Analytical and Experimental Investigation of Helicopter Rotor Hover Performance and Wake Geometry Characteristics*. USAAMRDL-TR, NTIS, 1971.
- [23] H. Glauert, *Airplane Propellers*, pp. 169–360. Springer Berlin Heidelberg, 1935.
- [24] W. Van Hoydonck, H. Haverdings, and M. Pavel, “A review of rotorcraft wake modeling methods for flight dynamics applications,” 2009.
- [25] D. Hidalgo Lopez, “Assessment of a state-space free wake for rotorcraft flight mechanics applications,” Master’s thesis, 2014.
- [26] E. Branlard, *Vortex Systems and Models of a Rotor —- Bound, Root and Wake Vorticity*, pp. 121–133. Cham: Springer International Publishing, 2017.
- [27] A. Conlisk, “Modern helicopter rotor aerodynamics,” *Progress in Aerospace Sciences*, vol. 37, no. 5, pp. 419 – 476, 2001.
- [28] T. Egolf, “Helicopter free wake prediction of complex wake structures under blade-vortex interaction operating conditions,” 1988.
- [29] R. T. N. Chen and A. R. Center., *A survey of nonuniform inflow models for rotorcraft flight dynamics and control applications [microform] / Robert T.N. Chen*. National Aeronautics and Space Administration, Ames Research Center, 1989.
- [30] G. Gaonkar and D. Peters, “Review of dynamic inflow modeling for rotorcraft flight dynamics,” *VERTICA.*, vol. 12, no. 3, pp. 213–242, 1988.
- [31] W. Van Hoydonck, “Literature survey on the simulation and handling qualities for helicopters operating near ship decks,” 2006.
- [32] H. Glauert, *The Elements of Aerofoil and Airscrew Theory*. Cambridge Science Classics, Cambridge University Press, 1983.

- [33] R. P. Coleman, A. M. Feingold, and C. W. Stempin, "Evaluation of the induced-velocity field of an idealized helicopter rotor," June 1945.
- [34] W. Castles, J. Henri, and D. Leeuw, "The normal component of the induced velocity in the vicinity of a lifting rotor and some examples of its application," in *Supersedes NACA TN 2912*, 1954.
- [35] W. Sears, "Potential flow around a rotating cylindrical blade," *Journal of the Aeronautical Sciences*, vol. 17, no. 3, pp. 183–184, 1950.
- [36] C. Lock, *Experiments to Verify the Independence of the Elements of an Airscrew Blade*. Aeronautical Research Committee reports and memoranda, H.M. Stationery Office, 1925.
- [37] P. Carpenter and B. Fridovich, *Effect of a Rapid Blade-pitch Increase on the Thrust and Induced-velocity Response of a Full-scale Helicopter Rotor*. National Advisory Committee for Aeronautics technical note, National Advisory Committee for Aeronautics, 1953.
- [38] D. Pitt, *Rotor Dynamic Inflow Derivatives and Time Constants from Various Inflow Models*. Defense Technical Information Center, 1980.
- [39] D. M. Pitt and D. A. Peters, "Theoretical prediction of dynamic-inflow derivatives," 1980.
- [40] D. A. Peters, "How dynamic inflow survives in the competitive world of rotorcraft aerodynamics," *Journal of the American Helicopter Society*, vol. 54, no. 1, p. 11001, 2009.
- [41] J. Zhao, *Dynamic wake distortion model for helicopter maneuvering flight*. PhD thesis, Georgia Institute of Technology, 2005.
- [42] K. R. Krothapalli, J. Prasad, and D. A. Peters, "Study of a rotor flap-inflow model including wake distortion terms,"
- [43] D. A. Peters and C. J. He, "Correlation of measured induced velocities with a finite state wake model," *Journal of the American Helicopter Society*, vol. 36, no. 3, pp. 59–70, 1991.
- [44] D. A. Peters and C. J. He, "Finite state induced flow models part ii: three-dimensional rotor disk," *Journal of Aircraft*, vol. 32, no. 2, pp. 323–333, 1995.
- [45] Z. Fei and Y. Zhang, "Three-dimensional dynamic inflow below the rotor disk based on the finite-state method," *Journal of Vibration and Control*, vol. 22, no. 16, pp. 3491–3503, 2016.
- [46] J. A. Morillo and D. A. Peters, "Velocity field above a rotor disk by a new dynamic inflow model," *Journal of aircraft*, vol. 39, no. 5, 2002.
- [47] D. A. Peters, A. Hsieh, and C. Garcia-Duffy, "A complete finite-state inflow theory from the potential flow equations," in *3rd International Basic Research Conference on Rotorcraft Technology, Nanjing, China*, 2009.
- [48] Z. Fei and D. A. Peters, "Fundamental solutions of the potential flow equations for rotorcraft with applications," *AIAA Journal*, vol. 52, pp. 1251–1261, 2014.
- [49] S. Goldstein, "On the vortex theory of screw propellers," *Proceedings of the Royal Society of London A: Mathematical, Physical and Engineering Sciences*, vol. 123, no. 792, pp. 440–465, 1929.
- [50] D. S. Jenney, J. H. Olson, and A. J. Landgrebe, "A reassessment of rotor hovering performance prediction methods," *Journal of the American Helicopter Society*, vol. 13, no. 2, pp. 1–26, 1968.

- [51] P. Li and R. Chen, "Rotor unsteady aerodynamics model using an efficient freevortex method," *Aircraft Engineering and Aerospace Technology*, vol. 84, no. 5, pp. 311–320, 2012.
- [52] D. R. Clark and A. C. Leiper, "The free wake analysis - a method for the prediction of helicopter rotor hovering performance," *Journal of the American Helicopter Society*, vol. 15, no. 1, pp. 3–11, 1970.
- [53] A. Bagai, J. G. Leishman, and J. Park, "Aerodynamic analysis of a helicopter in steady maneuvering flight using a freevortex rotor wake model," *Journal of the American Helicopter Society*, vol. 44, no. 2, pp. 109–120, 1999.
- [54] A. Bagai and J. G. Leishman, "Adaptive Grid Sequencing and Interpolation Schemes for Helicopter Rotor Wake Analyses," *AIAA Journal*, vol. 36, pp. 1593–1602, Sept. 1998.
- [55] M. J. Bhagwat and J. G. Leishman, "Stability, consistency and convergence of timemarching freevortex rotor wake algorithms," *Journal of the American Helicopter Society*, vol. 46, no. 1, pp. 59–71, 2001.
- [56] M. J. Bhagwat and J. G. Leishman, "Rotor aerodynamics during maneuvering flight using a timeaccurate freevortex wake," *Journal of the American Helicopter Society*, vol. 48, no. 3, pp. 143–158, 2003.
- [57] F. Palo, R. Mengotti, F. Scorcelletti, and L. Vigevano, "Fast free wake: a possible approach to real-time rotor wake simulation," *37th European Rotorcraft Forum 2011*, vol. 1, pp. 1109–1121, Sept. 2011.
- [58] S. Newman, *The foundation of helicopter flight*. Wiley, 1994.
- [59] W. Johnson, "Model for vortex ring state influence on rotorcraft flight dynamics," *AHS 4th Decennial Specialist's Conference on Aeromechanics, San Francisco, California*, January 2004.
- [60] P. E. I. Pounds, "Design, construction and control of a large quadrotor micro air vehicle," 2007. CD contains design files and data.
- [61] M. Bangura, M. Melega, R. Naldi, and R. Mahony, "Aerodynamics of rotor blades for quadrotors," *ArXiv e-prints*, January 2016.
- [62] R. Fox, A. McDONALD, and P. PRITCHARD, *Introduction to fluid mechanics, sixth edition*. John Wiley & Sons, INC., 2004.
- [63] J. Castles, Walter and R. B. Gray, "Empirical relation between induced velocity, thrust, and rate of descent of a helicopter rotor as determined by wind-tunnel tests on four model rotors," 1951.
- [64] P. Pounds, R. Mahony, J. Gresham, P. Corke, and J. M. Roberts, "Towards dynamically-favourable quad-rotor aerial robots," in *proc. of the Australasian Conference on Robotics and Automation 2004 ACRA2004* (N. Barnes and D. Austin, eds.), (Australian National University Canberra), Australian Robotics & Automation Association, December 2004.